



UNIVERSITÉ  
DE GENÈVE

FACULTÉ DES SCIENCES

Section de physique

---

PROBING HEAVY NEUTRAL LEPTONS  
IN THE  $ejj$  CHANNEL AT THE FCC- $ee$  :  
KINEMATIC SIGNATURES AND  
DISCOVERY POTENTIAL

---

Dimitri MOULIN

Supervised by

Anna SFYRLA and Pantelis KONTAXAKIS

21 juin 2023

## Abstract

The Future Circular electron-positron Collider (FCC-ee) is a proposed high luminosity particle accelerator for high precision measurements and possible discovery potential for new physics. Heavy Neutral Leptons (HNLs) are hypothetical particles with discovery potential at the FCC-ee which could provide explanations for several observations of physics beyond the Standard Model. This thesis focuses on the semi-leptonic decays of HNLs within the Phenomenological Type I Seesaw model, with one single HNL mixing with electron neutrinos only.

Two studies, the first exploring the sensitivity of the FCC-ee for HNLs and the second investigating its capacity to distinguish Dirac from Majorana HNLs, are introduced. Both studies are performed using the FCC-ee framework for the experimental run at the Z pole. The sensitivity study explores the signal significance against several generated background events and proposes an event selection optimized accross a range of HNL masses. The final result consists of a sensitivity plot as a function of mass and mixing angle. The Dirac versus Majorana study explores several jet-related kinematical variables for HNL masses of 20, 50 and 70 GeV with a mixing angle of  $V_{eN} = 10^{-3}$ . As a result, several discriminating variables are proposed as efficient discriminants.

# Summary

1	Introduction . . . . .	1
2	Background and litterature review . . . . .	3
2.1	Heavy Neutral Leptons . . . . .	3
2.1.1	Type I Seesaw model . . . . .	4
2.1.2	Feynman diagrams . . . . .	6
2.1.3	Solutions to Standard Model issues . . . . .	9
2.2	The FCCee . . . . .	11
2.2.1	The International Detector for Electron-positron Ac- celerators . . . . .	14
2.2.2	FCCee reach on HNLs . . . . .	15
3	Simulation setup . . . . .	17
3.1	Software setup . . . . .	17
3.2	Jet algorithm . . . . .	20
3.3	Signal samples . . . . .	21
3.4	Background samples . . . . .	22
4	Analysis . . . . .	24
4.1	Sensitivity analysis . . . . .	24
4.1.1	Sample normalization . . . . .	25
4.1.2	Significance . . . . .	26
4.1.3	Discriminating variables . . . . .	28
4.1.4	Event selection . . . . .	35

---

4.1.5	Results . . . . .	39
4.1.6	Outlook . . . . .	43
4.2	Dirac vs. Majorana discrimination . . . . .	44
4.2.1	Explored variables . . . . .	45
4.2.2	Discriminating variables . . . . .	53
4.2.3	Outlook . . . . .	61
5	Conclusion . . . . .	63
Appendix A . . . . .		65
Appendix B . . . . .		65
Appendix C . . . . .		67
References . . . . .		74

# 1 Introduction

The Standard Model (SM) is a very successful theoretical framework describing the elementary particles and their interactions. It has predicted the existence of the Higgs boson fifty years before its discovery and has been tested to the unequalled precision of  $\mathcal{O}(10^{-12})$  in its Quantum Electrodynamics (QED) predictions [30], [11]. However, the SM still appears to be incomplete as it lacks explanation for well-established observed phenomena, such as the lightness of neutrino masses, dark matter or the baryonic asymmetry of the Universe, among others.

The usual way to answer these questions is to introduce one or multiple new particles, possibly with new interacting mechanisms in order to reconcile theory and measurements. Consequently, the discovery of yet to be detected particles has to come with the design of more sensitive detectors or even better, new particle accelerators. The Future Circular Collider (FCC) at the CERN is without any doubt the most exciting project currently being discussed, as it promises to be the next world's largest particle accelerator. Its first phase, FCC-ee, will be focusing exclusively on electron-positron collisions and will offer an unmatched integrated luminosity of  $150 \text{ ab}^{-1}$  during its first four years of operation. This amount of statistics is perfect for high-precision studies of the SM, but can also be used for the direct discovery of feebly interacting particles.

Heavy Neutral Leptons (HNLs) are hypothetical particles with masses ranging from a few GeVs to several TeVs, which could provide crucial insights into the origin of neutrino masses, dark matter, and the matter-antimatter asymmetry conundrum. This thesis focuses on the semi-leptonic decays of HNLs in the context of the Phenomenological Type I Seesaw model and contains two studies. The first is a sensitivity analysis of HNLs in the FCC-ee framework, where the HNL signal is compared to multiple SM background samples and several event selections based on kinematical variables are proposed. The final results are presented in a sensitivity plot that explores the simulated parameter space of mass and mixing angles. The second study aims at evaluating the capacity to discriminate the Dirac from the Majorana nature of HNLs in the semi-leptonic channel within the FCC framework, and is the continuation of a previous study focusing on the fully-leptonic channel. As a result, several discriminating variables are proposed as efficient discriminants for HNL masses of 20, 50 and 70 GeV, with a mixing angle of  $V_{eN} = 10^{-3}$ .

This thesis is structured as follows. Section 2 outlines the theoretical background behind the analyses. Section 3 describes the specifics of event generation and simulation in the FCC framework. Sections 4.1 and 4.2 contain the core of the sensitivity and Dirac vs. Majorana analysis, respectively. Finally, the conclusion is presented in Section 5.

## 2 Background and literature review

This section aims at giving the reader a comprehensive overview of the theoretical framework behind these analyses. It contains a short description of HNLs in the context of the Phenomenological Type I Seesaw model which gives rise to Dirac and Majorana HNLs, and a brief overview of FCC-ee and its potential reach on HNLs.

### 2.1 Heavy Neutral Leptons

The observation of neutrino flavor oscillations [20], [19] can be elegantly explained by admitting that the Standard Model (SM) neutrinos have nonzero mass through the Pontecorvo–Maki–Nakagawa–Sakata (PMNS) [32] mixing matrix. These observations directly contradict the original SM assumption that neutrinos are massless particles. An extension of the SM is thus necessary to account for these nonzero neutrino masses. One simple and elegant extension of the SM which accounts for the small but nonzero mass of SM neutrinos is the introduction of Heavy Neutral Leptons (HNLs), also referred to as sterile neutrinos. These HNLs are the right-handed partners of the exclusively left-handed SM neutrinos and have no electric, weak or color charge. Hence, they can only interact via their coupling to the Higgs field and to SM neutrinos, generating their small masses via the so-called Seesaw mechanism [33]. There are many different versions of Seesaw models, which can greatly vary in their implementation and complexity [5], as well as in the physics scale they are pro-

bing. The common minimal implementation of these Seesaw models are the Type I, Type II and Type III Seesaw models, which can then be extended towards more complex theories. For this thesis, we focus on the benchmark Type I Seesaw model, which we will now describe.

### 2.1.1 Type I Seesaw model

In Type-I Seesaw models, the SM is extended by the introduction of  $\mathcal{N}$  right-handed fermions (which we identify as HNLs) that couple to the SM neutrinos in the same way as the coupling between the left — and right — handed components of charged leptons. For the Type-I Seesaw model, the interaction terms between the HNLs ( $N_i$ ) and the Z, W and Higgs ( $H$ ) bosons in the Lagrangian are given by [12]

$$\mathcal{L}^{int} = \mathcal{L}^W + \mathcal{L}^Z + \mathcal{L}^H \quad (1)$$

with

$$\mathcal{L}^Z = -\frac{g_W}{2\cos\theta_W} \sum_{l=e}^{\tau} \sum_{i=1}^{n_s} \bar{N}_i V_{li}^* Z_\mu \gamma^\mu P_L \nu_L + \text{h.c} \quad (2)$$

$$\mathcal{L}^W = -\frac{g_W}{\sqrt{2}} \sum_{l=e}^{\tau} \sum_{i=1}^{n_s} \bar{N}_i V_{li}^* W_\mu^+ \gamma^\mu P_L l^- + \text{h.c} \quad (3)$$

$$\mathcal{L}^H = -\frac{g_W}{2M_W} h \sum_{l=e}^{\tau} \sum_{i=1}^{n_s} \bar{N}_i V_{li}^* m_{N_i} P_L \nu_l + \text{h.c} \quad (4)$$

As these HNLs are singlets under the gauge symmetries of the SM,  $U(1) \times SU(2) \times SU(3)$ , a Majorana mass term is also allowed. In that case, we have have



two mass terms, one Dirac mass ( $m_D$ ) term formed between the regular neutrinos and the HNL, and a Majorana mass term ( $M$ ) involving only the HNL ( $N_R$ ) :

$$m_D \overline{\nu_L} N_R + h.c \quad M \overline{(N_R)^C} N_R + h.c \quad (5)$$

For simplicity, we consider the case of a single  $\nu$  and  $N$ . The same logic can be applied to include three neutrinos and an arbitrary number of  $N$ . We can then write a combined Dirac-Majorana mass term using a neutrino mass matrix as :

$$\begin{pmatrix} \overline{\nu_L^C} & \overline{N_R} \end{pmatrix} \begin{pmatrix} 0 & m_D \\ m_D & M \end{pmatrix} \begin{pmatrix} \nu_L \\ N_R^C \end{pmatrix} \quad (6)$$

This matrix can then be diagonalized in order to obtain the mass eigenstates of the left — and right — handed neutrinos [28]. Assuming  $m_D \ll M$ , which can be described as the Seesaw mechanism condition, the mass eigenstates are then derived as :

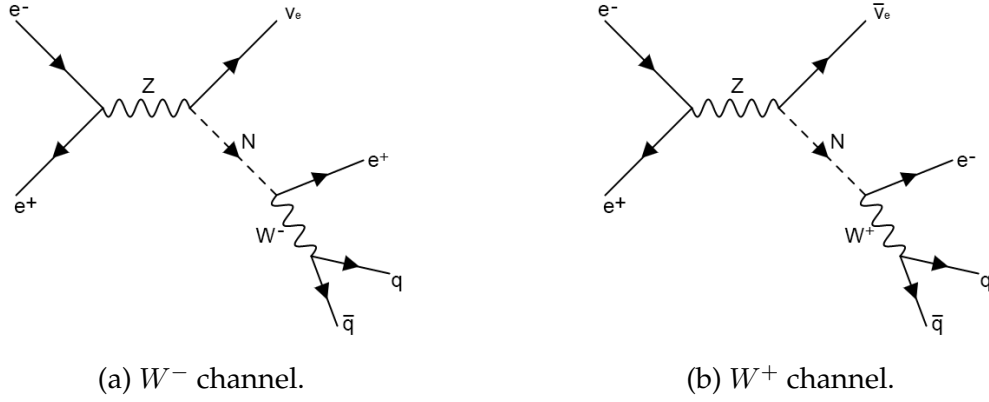
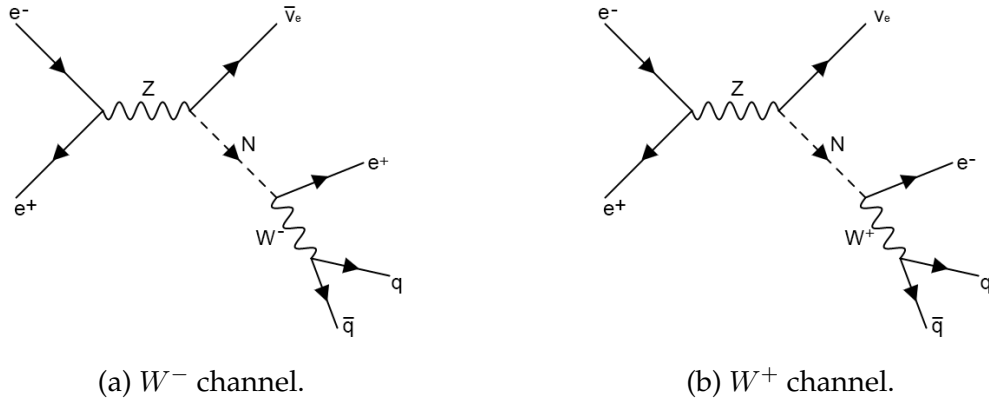
$$m_\nu \approx \frac{m_D^2}{M} \quad m_N \approx M \quad (7)$$

Thus, in the Seesaw mechanism,  $m_\nu$  is suppressed by the large value of  $M$  over  $m_D$ . This mechanism provides a natural explanation for the lightness of neutrino masses, as the Dirac mass is presumably generated via the Higgs mechanism and would be of the same order as the mass of a quark or a charged lepton (in the same generation of the neutrino we are considering). Note that in this benchmark model, the mixing

angle and the HNL mass are taken to be independent from each other. Depending on the physical phenomenon to be accounted for, one can find strong constraints on the mixing angle and mass of the HNL. For simplicity, this analysis considers only the lightest HNL mixing only with electron neutrinos,  $N_1$ , denoted by  $N$ , with mass and mixing  $m_N$  and  $V_{eN}$ . We further emphasize that considering only one HNL is for bench-marking and studying purposes only, as more realistic scenarios usually contain multiple mass eigenstates.

### 2.1.2 Feynman diagrams

In principle, the Feynman rules can then be determined from the Lagrangian given in equation [1], keeping in mind that additional rules apply for Majorana particles as these allow lepton number violating (LNV) decays in addition to lepton number conserving (LNC) decays. In our case, we will leave the Feynman rules to the theorists, and will focus on the Feynman diagrams and branching ratios corresponding to our processes of interest. In general, the HNL can be produced from  $Z$ ,  $W$  or Higgs-boson decays through mixing with the SM neutrinos. For this analysis, we will be focusing on semi-leptonic decays of HNLs produced in the  $Z$ -channel. As mentioned earlier, Majorana HNLs allow for lepton number violating decays, so these will possess twice as many diagrams as the Dirac ones (both LNC and LNV). Figures [1] and [2] show the different Feynman diagrams of interest.

Figure 1 LNC diagrams for the  $e\nu jj$  channelFigure 2 LNV diagrams for the  $e\nu jj$  channel

The decay width of  $Z \rightarrow \nu_i N_j$  depends on the specific coupling between the HNL and the SM neutrinos states which is denoted by  $\theta_{ij}$ , with  $i = e, \mu, \tau$ , and  $j = 1, 2$ , corresponding to the sterile neutrino. Neglecting the masses of the light neutrinos and charged leptons, the decay rate reads [10] :

$$\begin{aligned}
 \Gamma(Z \rightarrow \bar{\nu}_i N_j) &= |\theta_{ij}|^2 \cdot \Gamma(Z \rightarrow \nu_i \bar{\nu}_i) \cdot \Pi\left(\frac{M_N}{m_Z}\right) \\
 &= |\theta_{ij}|^2 \cdot \frac{G_F m_Z^3}{6\sqrt{2} \cdot \pi} \cdot \Pi\left(\frac{M_N}{m_Z}\right)
 \end{aligned} \tag{8}$$

Where  $|\theta_{ij}|^2 = \sum_{i,j} \theta_{ij}^2$ ,  $G_F$  is the Fermi coupling constant, and the phase space factor is given by

$$\Pi \left( \frac{M_N}{m_Z} \right) = \frac{1}{2} \left( 1 - \frac{M_N^2}{m_Z^2} \right)^2 \left( 1 + \frac{M_N^2}{2m_Z^2} \right) \quad (9)$$

Note that the decay rates of  $Z$  to  $N$  are the same as the ones to  $\bar{N}$ , i.e.  $\Gamma(Z \rightarrow \nu_i \bar{N}_j) = \Gamma(Z \rightarrow \bar{\nu}_i N_j)$ . The HNL can then decay through the same channels as they can be produced. In particular, the decay rate for the HNL decaying to two quarks and a charged lepton via a  $W$ -boson,  $\Gamma(N \rightarrow l^\pm q \bar{q}')$  is given by :

$$\Gamma(N \rightarrow l_\alpha^\pm q \bar{q}') = \frac{1}{2} |\theta_\alpha|^2 \frac{G_F M_N^3}{4\sqrt{2} \cdot \pi} \Gamma(W \rightarrow q \bar{q}') \cdot \frac{1}{2} \left( 1 - \frac{m_Z^2}{M_N^2} \right)^2 \left( 1 + \frac{2m_Z^2}{M_N^2} \right) \quad (10)$$

A typical signature of a visible decay from an HNL in the semi-leptonic channel would then be characterised by a di-jet system associated to the quark pair, as well as an isolated charged lepton ( $e^\pm$  in this analysis), with missing momentum from the neutrino.

**Lifetime** While the number of HNLs produced in  $Z$ -decays along with a lepton or antilepton of a given flavour is the same for Dirac and Majorana HNLs, their decay rates differ by a factor two due to LNV decays being allowed for Majorana HNLs. The total decay rate can be written as [24] :

$$\Gamma_N \approx c_{dec} \frac{a}{96\pi^3} U^2 M_N^5 G_F^2 \quad (11)$$

with  $a \approx 12$  for  $M_N < M_Z$  and  $c_{dec}=1$  ( $c_{dec}=1/2$ ) for Majorana (Dirac). The corresponding decay length is then

$$\lambda_N = \frac{\beta\gamma}{\Gamma_N} \approx \frac{1.6}{U^2 c_{dec}} \left( \frac{M_N}{\text{GeV}} \right)^{-6} \left( 1 - \left( \frac{M_N}{m_Z} \right)^2 \right) \text{cm}. \quad (12)$$

Therefore — in this simplified scenario — one could unambiguously distinguish Dirac from Majorana HNLs by determining  $c_{dec}$ . In more realistic models, with  $n_{HNL} > 1$ , the situation is more complicated, see [6] for more details.

### 2.1.3 Solutions to Standard Model issues

In addition to providing an explanation for the non-zero (but extremely small) neutrino mass, HNL theories can also provide answers to two other fundamental questions, namely the Baryonic Asymmetry of the Universe, and Dark Matter. We give a small description of both in the next paragraph.

Our universe appears to be largely dominated by matter, rather than anti-matter<sup>1</sup>. However, the SM hardly favors matter over anti-matter, as the few times where it is the case is through very rare processes allowing for CP violations, which are not enough to explain the abundance of matter over anti-matter, also referred to as the Baryonic Asymmetry of the Universe (BAU). Leptogenesis describes the asymmetry of leptons and anti-leptons in the early universe, and proposes an interesting

---

1. Or vice versa, as we could call matter anti-matter and we would live in a Universe dominated by the latter.

solution to the BAU, by linking it to the origin of light neutrino masses [4]. In this scenario, the same HNLs responsible for the light neutrino masses can produce the matter-anti-matter asymmetry via their CP violating decays in the early Universe [26]. The most popular scenario is based on the Type I Seesaw described in section [2.1.1], where the SM is simply extended by at least two HNLs. It is now understood that HNL masses in the dozens of GeVs have the ability to generate leptogenesis, making FCC-ee an excellent laboratory to study their properties and test their connection to the BAU.

Dark Matter (DM) is also a very notorious open question both in particle physics and cosmology. According to various independent cosmological measurements [18], only 5% of the universe consists of baryonic matter (i.e. matter as we know it), while there would be about 27% of DM and 68% of dark energy. From the particle physics point of view, a dark matter candidate would be a very weakly interacting particle that does not interact with photons, such that it does not emit or absorb any light. It turns out that HNLs with sufficiently small masses and couplings could constitute a viable (warm) DM candidate [23]. Depending on the HNL model such as  $\nu$ MSM [36], or models where HNLs have additional gauge interactions [34], in which HNLs are viable<sup>2</sup> DM candidates, FCC-ee could provide an efficient environment for direct discovery or for probing the sector around their production.

---

2. *Viable* meaning candidates which successfully reproduce physical observations.

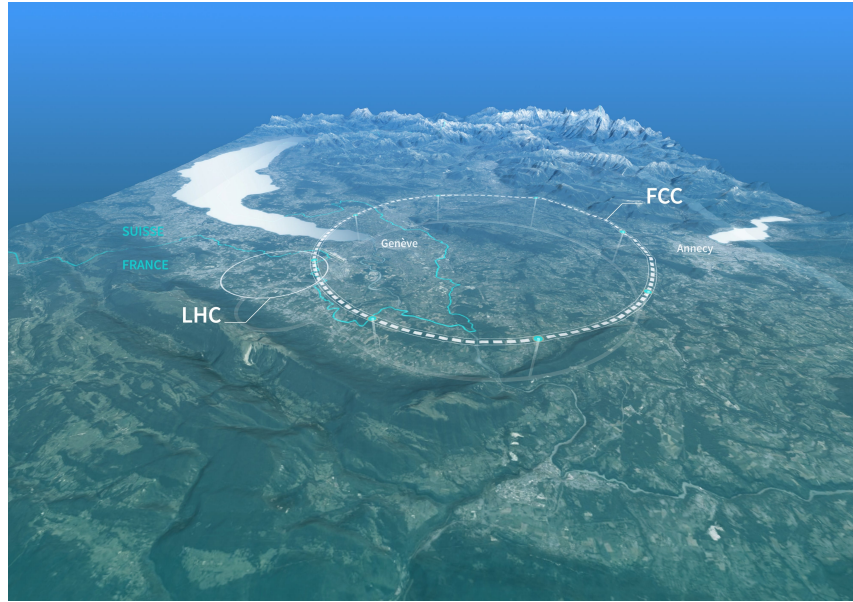


Figure 3 Artistic map showing the proposed FCC location and relative size compared to the LHC, close to the French-Swiss frontier. (Image :CERN)

## 2.2 The FCCee

The Future Circular Collider (FCC) program is a design study for a future particle accelerator at the CERN, succeeding to the Large Hadron Collider (LHC) as the largest particle accelerator in the world, with a circumference of about 100km built around the CERN area, as can be seen from figure [3]. The FCC is currently proposed as a two-stages project, with a first lepton collider phase (FCC-ee) with a focus on precision measurements of electroweak parameters in the SM, including Higgs properties [13]. It will be followed by a subsequent higher-energy hadron collider (FCC-hh) with a center of mass energy of 100TeV, aiming for direct discoveries of new phenomena. It is anticipated that most of the infrastructure of FCC-ee could be reused by FCC-hh, similarly to how the LHC inherited a part of the Large Electron Positron (LEP) infrastructure back in the day.

The FCC-ee will be a very high luminosity electron-positron collider, which purpose is to study with high precision the  $Z$ ,  $W$ , Higgs and top particles. It will therefore cover a wide energy range of 90 - 365 GeV, going through different stages starting from the  $Z$ -pole, over to the  $WW$  threshold and Higgs production peak, up to the top-pair threshold. It is estimated that FCC-ee will produce samples of  $5 \cdot 10^{12}$   $Z$ -bosons,  $10^8$   $W$  pairs,  $10^6$  Higgs bosons and  $10^6$  top quarks pairs [3]. One significant advantage of electron-positron colliders is the elementary nature of the collided particles. Contrary to hadronic events (e.g from a proton-proton collision), leptonic and semi-leptonic events are much easier to study, as these benefit from low pile-up collisions and the absence of any underlying event, with one major advantage being that the energy and momentum of the initial and final states are known.

There are several advantages to the FCC-ee being a circular collider, rather than a linear collider, like the Compact Linear Collider (CLIC). The main advantage of a circular collider is the luminosity gained by the presence of two interaction points. Figure [4] shows a comparison between several proposed colliders (both linear and circular) and FCC-ee [13]. Another advantage of circular colliders is the possibility to use the transverse polarisation of the stored beams for beam energy calibration, allowing the centre-of-mass energy to be determined with high precision.

Therefore, the design of FCC-ee as a circular collider appears to efficiently fulfill its physics requirements of being a high luminosity, high precision laboratory for testing the SM.

On the other hand, one should note that a major pitfall of circular electron-



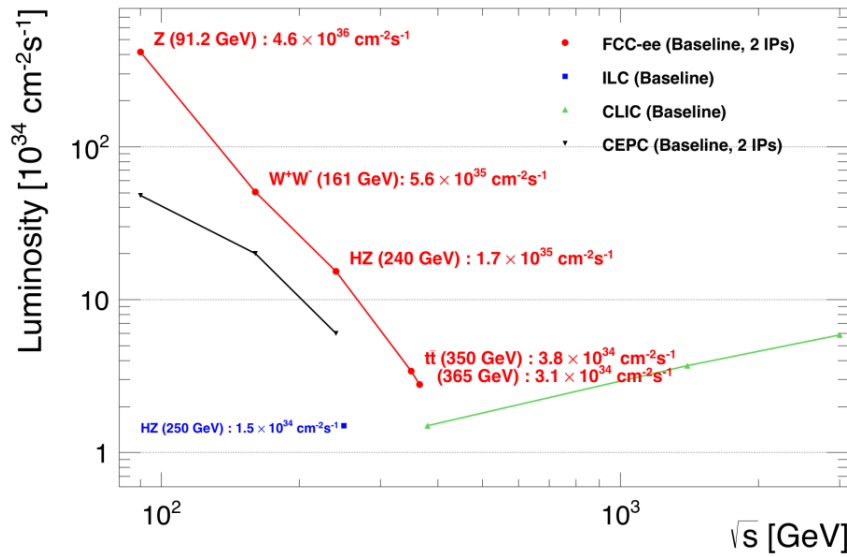


Figure 4 : FCC-ee baseline luminosities summed over all interaction points as a function of the centre-of-mass energy ( $\sqrt{s}$ ), compared to other e+e- collider proposals (ILC, CLIC, and CEPC).

positron colliders is the upper threshold on the beam energy around 200 GeV, due to synchrotron radiation. Indeed, all charged particles lose energy when their trajectory is deflected by a magnetic field, and the energy loss is proportional to  $\gamma^4$ <sup>3</sup>. As electrons are the lightest particles in the SM (neutrinos excluded), their  $\gamma$  factor is very large, resulting in a high synchrotron radiation. However, it is still possible to attain a high center of mass energy in  $e^+e^-$  collisions using a linear collider. Therefore, high precision measurements can be attained with circular colliders such as the FCC-ee, and high centre of mass energy can be obtained with linear lepton colliders.

---

3.  $\gamma$  is the Lorentz factor

### 2.2.1 The International Detector for Electron-positron Accelerators

Two complementary detector designs, the CLIC-Like Detector (CLD) and the International Detector for Electron-positron Accelerators (IDEA) are being studied for the FCC-ee. As its name suggests, the CLD uses a similar detector design as the CLIC at the CERN, while the IDEA is a new concept, developed specifically for the FCC-ee. As this thesis uses the IDEA for the simulating the detector response, we will now give a short description of it.

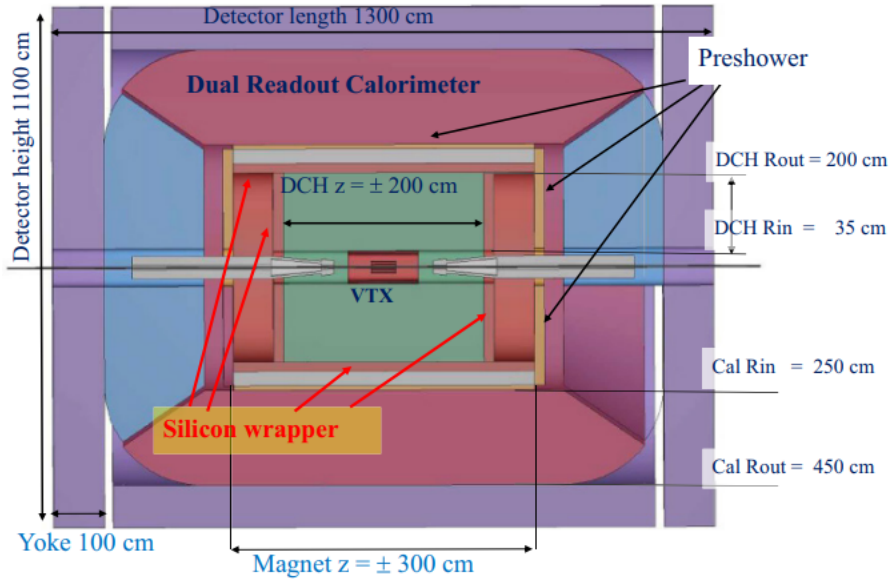


Figure 5 Schematic layout of the IDEA detector [3].

The structure of the detector is outlined in figure [5]. The detector is composed of a silicon pixel vertex detector (VTX) in the innermost layer. It is surrounded by a large-volume short-drift wire chamber (DCH) characterised by a high transparency in terms of radiation lengths, and is designed to provide good tracking, high-precision momentum measurement and excellent particle identification by cluster

counting<sup>4</sup>[27]. The electric field in the DCH is generated by a thin, low-mass superconducting solenoid coil, used to bend the charged particles in order to measure their momenta. The DCH is surrounded on the outside by a layer of silicon micro-strip detectors, which allows to increase momentum resolution and extend the tracking coverage in the forward/backward region.

The outter region of the detector is then composed of a pre-shower detector, a dual-readout calorimeter and muon chambers within the magnet return yoke. The pre-shower detector is intended to enhance the performance of the calorimeter in accurately distinguishing photons from electrons. The dual-readout calorimeter, which aim is to measure the energy of the particles coming through, is sensitive to the independent signals from scintillation and cherenkov light [3].

### 2.2.2 FCCee reach on HNLs

The FCC-ee shows a great sensitivity to study HNLs in the kinematically accessible regime [25]. Figure [6] shows an estimation of different discovery regions for several proposed detectors and setups, depending on the electron-mixing angle  $\Theta$  [4] and mass of the HNL  $m_N$ .

---

4. Cluster counting is when particles originating from the same decay are clustered together to reconstruct the complete decay process.

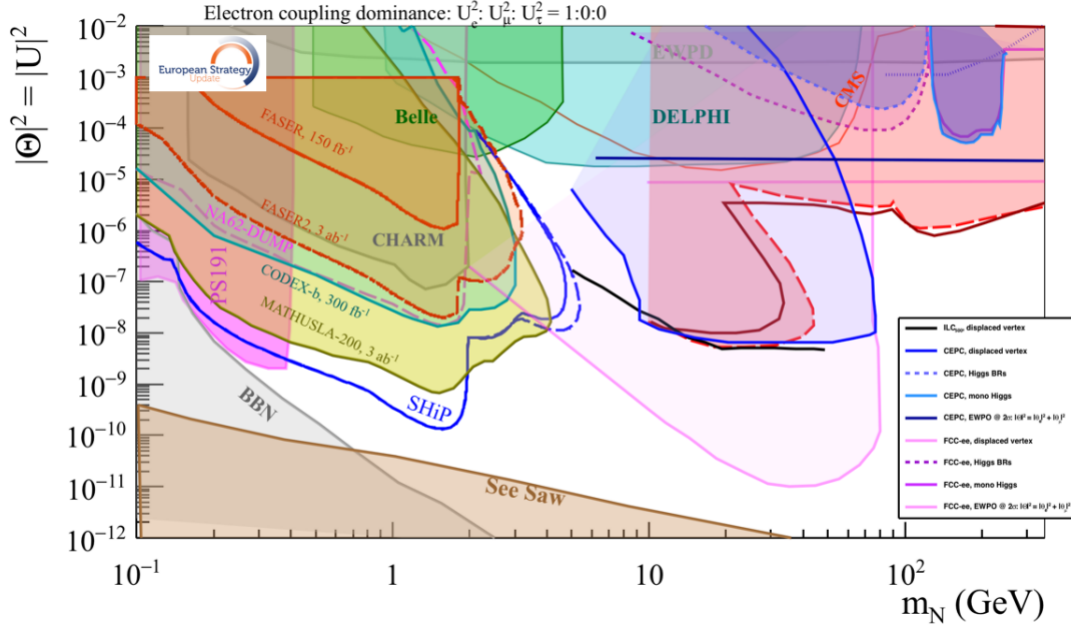


Figure 6 90% CL exclusion limits for a Heavy Neutral Lepton mixed with the electron neutrino, as presented in the European Strategy for Particle Physics Briefing Book [25]. The FCC-ee curves are in (overlined) dark purple. The curve below the Z boson mass corresponds to the combined LLP and prompt analysis performed with  $10^{12}$  in Ref. [9]. The horizontal limit at high masses results from the effect of light-heavy neutrino mixing on the EW precision observables.

As mentioned before, this thesis assumes a simple phenomenological model (1), with  $\mathcal{N}_{\mathcal{HNL}} = 1$ , i.e., only one HNL that is either a Dirac or Majorana fermion. It is therefore useful to take a look at the expected number of events, given the target luminosity of the FCC-ee at the Z-pole of  $150\text{ab}^{-1}$ . Table [1] shows the expected number of events per cross-section<sup>5</sup> for an HNL with a mass  $m_N = 50\text{ GeV}$  in the channels shown in figure [1], for several choices of mixing angle  $|V_{eN}|$ . Looking at the expected number of events at the FCC-ee, it is clear that it provides a solid environment to the search for Heavy Neutral Leptons for a large parameter space.

5. The cross-sections here are computed by MadGraph using the computational setup described in section 3.

Mixing angle $ V_{eN} ^2$	Cross-section $\sigma$ [pb]	Expected events at $150 \text{ ab}^{-1}$
$10^{-4}$	$2.26 \times 10^{-1}$	33,900,000
$10^{-5}$	$2.26 \times 10^{-2}$	3,390,000
$10^{-6}$	$2.26 \times 10^{-3}$	339,000
$10^{-7}$	$2.26 \times 10^{-4}$	33,900
$10^{-8}$	$2.26 \times 10^{-5}$	3390
$10^{-9}$	$2.26 \times 10^{-6}$	339
$10^{-10}$	$2.26 \times 10^{-7}$	33.9

TABLE 1 Cross-section and expected number of events for  $150 \text{ ab}^{-1}$ . The results are shown for a Dirac HNL of mass 50GeV, and several mixing angles  $|V_{eN}|$ .

### 3 Simulation setup

This section presents the specific tools and methods which have been used in order to simulate and analyse the signals and backgrounds samples for this analysis. It starts with an overview of the software setup, followed by a description of the jet algorithm used in this analysis, and ends with the definition of the signal and background samples.

#### 3.1 Software setup

There are several steps to follow in order to simulate and run the analysis over the signal and background events. First, the events are generated by a Monte-Carlo generator where the specifics of the processes to be simulated are specified. Then, hadronization, parton shower simulation and detector response are implemented, producing the final nTuples. These nTuples are then to be analysed within the FCC-framework. An overview of these specific steps is shown in figure [7].

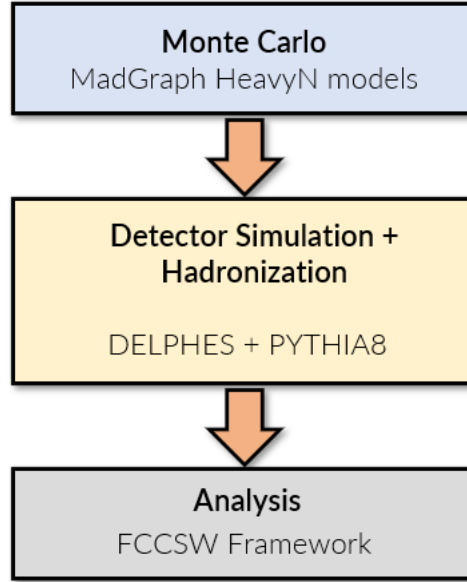


Figure 7 A simplified diagram of the simulation setup.

Events are first simulated using `MadGraph5_aMC@NLO v.2.6.7` [39][8], which produces Monte Carlo generated events according to the specified processes, particle properties (mass, coupling, etc..) and the corresponding model to consider (SM, SuSy, etc..). For the HNL events, the `HeavyN Universal FeynRules Object (UFO)` models are used, in particular, we use the `SM_HeavyN_Dirac_CKM_Masses`[35] and `SM_HeavyN_CKM_AllMasses` [22] [7] models respectively for Dirac and Majorana HNLs events generation. These models implement an extension of the SM with the addition of the Lagrangian described in [1] and allow us to simulate both LNC and LNV processes for Dirac and Majorana HNLs respectively. The properties of the HNL (mass and coupling), specific processes, as well as simulation properties (number of events, beam energy, etc..) are specified in a process card (also referred to

as proc. card). An example of proc. cards for Dirac HNLs events generation is given in [Appendix A](#). The output from MadGraph is a Les Houches Event (LHE) file that contains the relevant information concerning the processes and parameters used in the simulation.

The next step is to simulate the response from the detector as well as the shower and hadronisation processes. Both these steps are implemented together, using PYTHIA [38] and DELPHES [21]. Both DELPHES and PYTHIA use proc. cards to define the specifics of the simulations — examples of each can easily be found online. PYTHIA is used to simulate several physics processes such as the generation of hard scattering processes, parton showers, hadronization and the decay of unstable particles. DELPHES is designed to simulate the response of the IDEA detector described in section 2.2.1, through another proc. card containing the specific settings for the response of the detector. It takes into account effects like energy resolution, particle identification and event reconstruction. The final output is an EDM4HEP format file [40] which contains all the relevant information about the particles produced, including their momenta, energies, charges and particle identification. Even jets can be built by defining these in the proc. cards. In this analysis, the jets were built at the next step : the analysis level. The EDM4HEP format files are then analysed using the FCC analysis framework, which is based on RDataFrames [29], where C++ code is compiled in a ROOT [15] dictionary. These are then called using custom Python scripts.

## 3.2 Jet algorithm

As mentionned before, the jets can generally be computed and reconstructed by PYTHIA, by specifically defining the object in the PYTHIA process card. However, it is also possible to build the jets at the analysis level, directly from the particles objects in the EDMHEP file, allowing for more control and flexibility. In this thesis, the latter option was explored using the FastJet [16] external package. The jets were built at the analysis level, using an updated version of the Durham jet algorithm [17] of which we will now give a short description.

The goal of a jet algorithm is to cluster particles that are "close" together into a single object, corresponding to a particle jet. However, the notions of "closeness" and "distance" can be defined in different ways. In the case of the DURHAM algorithm, the distance measure is defined as the ratio of the squared invariant mass of the pair of particles to the total squared invariant mass of the event. This distance is then computed between every pair of particles, and the particles with the smallest distances are merged together into a jet. Then, the distances are updated between the merged jet and all the other particles. The merging procedure is then repeated until a stopping criterion is met. In our case, since the process we are interested in consists in its final state of one electron (positron) and two jets, the algorithm is setup to build exactly two jets in every event.



One important distinction, which is the reason for running this algorithm at the analysis level is that we explicitly removed the electrons (positrons) from the particle collection to be considered when building the jets with the DURHAM algorithm. In that way, the — reconstructed — electron (positron) is never part of the jet. Therefore the output jets from the algorithm are more likely to correspond to the same jets as the ones from the process of interest defined in [13].

### 3.3 Signal samples

To study Dirac and Majorana HNLs, the processes

$$\textbf{Dirac HNL : } e^+e^- \rightarrow Z \rightarrow N\bar{\nu}_e \ (\bar{N}\nu_e), \text{ with } N(\bar{N}) \rightarrow e^-(e^+)jj \quad (13)$$

$$\textbf{Majorana HNL : } e^+e^- \rightarrow Z \rightarrow N\bar{\nu}_e \ (N\nu_e), \text{ with } N \rightarrow e^-(e^+)jj \quad (14)$$

are simulated using the software described in section 3.1. The corresponding Feynman diagrams are shown in figure [1] for the Dirac case, which only permits LNC channels. For the Majorana case, both LNC [1] and LNV [2] channels are permitted. For the sensitivity study, the results consider Dirac HNLs only. Note that in principle, the HNL can also be produced via the Higgs boson, such that the Z could be replaced by a Higgs in equations [13] and [14]. However, as the Higgs boson is much heavier than the Z boson, the Higgs processes are suppressed and we can safely neglect its contribution.

For the sensitivity study, signals are generated with 100000 total number of raw

events, with masses of  $m_N = 10 - 80$  GeV in steps of 10 GeV, and electron mixing angles of  $|V_{eN}|^2 = 10^{-4} - 10^{-10}$ .

The Dirac vs. Majorana discrimination study focuses on HNL masses of  $m_N = 20, 50$  and 70 GeV, with mixing angle  $|V_{eN}|^2 = 10^{-6}$  and uses samples of  $N = 100000$  events both for Dirac and Majorana HNLs.

### 3.4 Background samples

In general, any SM process that can mimic the signal signature, either through a similar final state (irreducible background) or because of mislabeling/misreconstruction of the particles, is considered as background. For the sensitivity study, several backgrounds are considered. The background corresponding to the production of a Z boson decaying into two b-quarks, two c-quarks, as well as the 4-body decay producing the same final state as the signal, are considered in this analysis. Examples of Feynman diagrams for the Z to bb and the 4-body are shown in figure [8]. Note that these are just examples, as many other diagrams can lead e.g. to the  $e\nu qq$  final state.

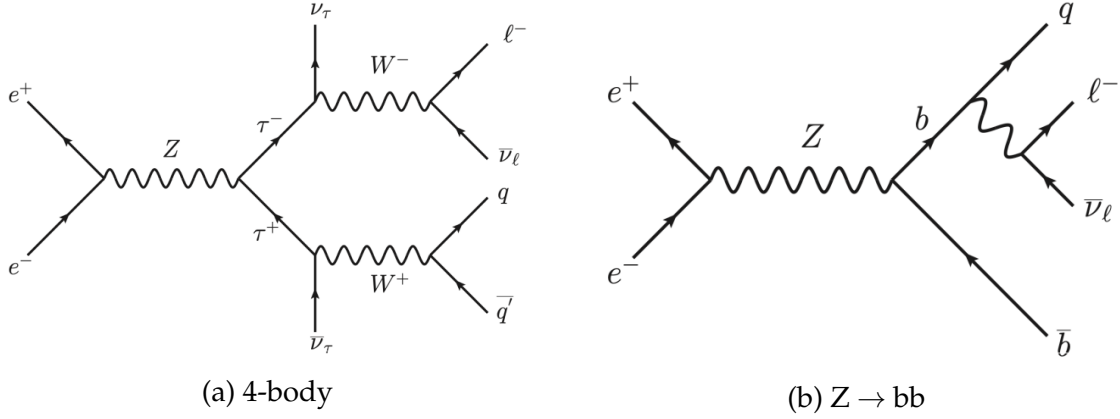


Figure 8 Feynman diagrams of two of the background processes.

The 4-body background was produced using the same procedure described in section 3.1 with the process card given in [Appendix B](#). The other background samples were generated in the Winter 2023 production campaign [1], with a similar setup as described before. Table [2] gives a summary of the background events, with their respective total number of raw events produced.

Process	$Z \rightarrow b\bar{b}$	$Z \rightarrow c\bar{c}$	4-body
Number of events	$438 \times 10^6$	$499 \times 10^6$	$10^5$

TABLE 2 Summary table of the total number of background events.

By taking a look at the Feynman diagrams from figure [8], we can see that the backgrounds can mimic the final state of our signal described in equation [13] through rather "rare" decays (electrons are found in b-jets about 5% of the time (NEED REF)). So one could conclude that selecting only events with high energy electrons would almost completely remove the background. However, one must

consider the cross-section differences between signal and background. From table [1], we can see that the typical cross-section for the signal lies in the range  $10^{-1} - 10^{-10}$  pb, while the cross-section for  $Z \rightarrow b\bar{b}$  is about  $10^3$  pb, therefore compensating for the rarity of the background process. This means that additional selections must be applied to improve the signal significance over the background. These selections are described in section 4.1.4.

## 4 Analysis

This analysis is separated into two subsections. The first is based on a sensitivity study at the FCC-ee of the semi-leptonic Dirac HNL signal with respect to the backgrounds presented in section 3.4. The second part of the analysis investigates our capacity to distinguish Dirac from Majorana HNLs at the FCC-ee in the semi-leptonic channels, if these were to be discovered. In both of these analyses, the signals include only one HNL mixing exclusively with electron neutrinos. A more complete analysis could include several HNLs mixing with different lepton families.

### 4.1 Sensitivity analysis

The purpose of this analysis is to determine if one could extract enough signal significance out of the background. The parameters of this analysis were tuned for HNL masses of 20, 50 and 70 GeV, with a mixing angle of  $|V_{eN}|^2 = 10^{-6}$  and was then extended to masses in the range 10-80 GeV, with a mixing angle in the range

$|V_{eN}|^2 = 10^{-4} - 10^{-10}$ . It starts with a description of the samples normalization, followed with the definition of significance which allows us to select discriminating variables to apply efficient selection cuts, presented in section 4.1.4. Finally, results are shown in the form of a contour plot, defining a range of mass/coupling pairs for which satisfying significance was attained.

#### 4.1.1 Sample normalization

At every step of the event selection, the number of events are normalized in order to replicate the expected integrated luminosity in the Z pole run at the FCC-ee. The current estimation is that the Z pole run will have a luminosity of  $L_{int} = 150\text{ab}^{-1}$ . Hence, the number of events is normalized using the total number of generated events  $N_{tot}$ , the process cross-section  $\sigma$  and the number of events remaining within a given selection  $n_{sel}$ , according to equation [15] :

$$n = \frac{\sigma \cdot L_{int}}{N_{tot}} n_{sel} \quad (15)$$

The aim of sample normalization is to be able to replicate the FCC-ee conditions as accurately as possible. However, considering the gigantic luminosity of the FCC-ee ( $150\text{ ab}^{-1}$  is 50 times larger than the target integrated luminosity of the High Luminosity LHC phase), this can cause issues with respect to the uncertainties after each selection. Indeed, we are working with about  $10^8$  simulated background events, which is 2000 times smaller than what is predicted for the FCC-ee (ideally, the simu-

lation statistics should be at least of the same order of magnitude as real data). For this reason, most of the analysis is performed with a target luminosity of  $10 \text{ fb}^{-1}$ , and we only scale to the full integrated luminosity of  $150 \text{ ab}^{-1}$  in the final result.

#### 4.1.2 Significance

In particle physics, the concept of significance refers to the statistical measure used to determine the credibility of experimental result. It quantifies the likelihood that the observed data deviates from the expected background, indicating the presence of a genuine signal or new phenomenon.

Significance is typically expressed in terms of standard deviations, known as sigma ( $\sigma$ ), where a higher sigma corresponds to a lower probability of obtaining the observed result by chance alone, thereby increasing confidence in the validity of the results. There are multiple ways of calculating the significance depending on the hypothesis [2]. While a significance of  $5\sigma$  is typically considered to be the threshold for claiming a discovery, a significance of  $2\sigma$  is often used as an indication of interesting or potentially intriguing results and can help identify promising trends or features in the data which could be overlooked by a  $5\sigma$  threshold. In this analysis, the significance of observing  $n$  events given a prediction of  $b \pm \sigma$  events is computed according to the recommended formula in [2] :

$$Z = \sqrt{2 \left( n \cdot \ln \left[ \frac{n(b + \sigma^2)}{b^2 + n\sigma^2} \right] - \frac{b^2}{\sigma^2} \ln \left[ 1 + \frac{\sigma^2(n - b)}{b(b + \sigma^2)} \right] \right)} \quad (16)$$

Where  $\sigma$  is the uncertainty on the background, taken to be 10% throughout this analysis. In particular, we will compute the cumulated significance for the histogram bins of several variables in order to identify the selections that preserve the most significance of signal versus background. One careful thing to consider when computing the cumulative significance is whether the events to preserve are to the left or to the right of the cut. We give a quick example to illustrate this : consider the two distributions given in figure [9].

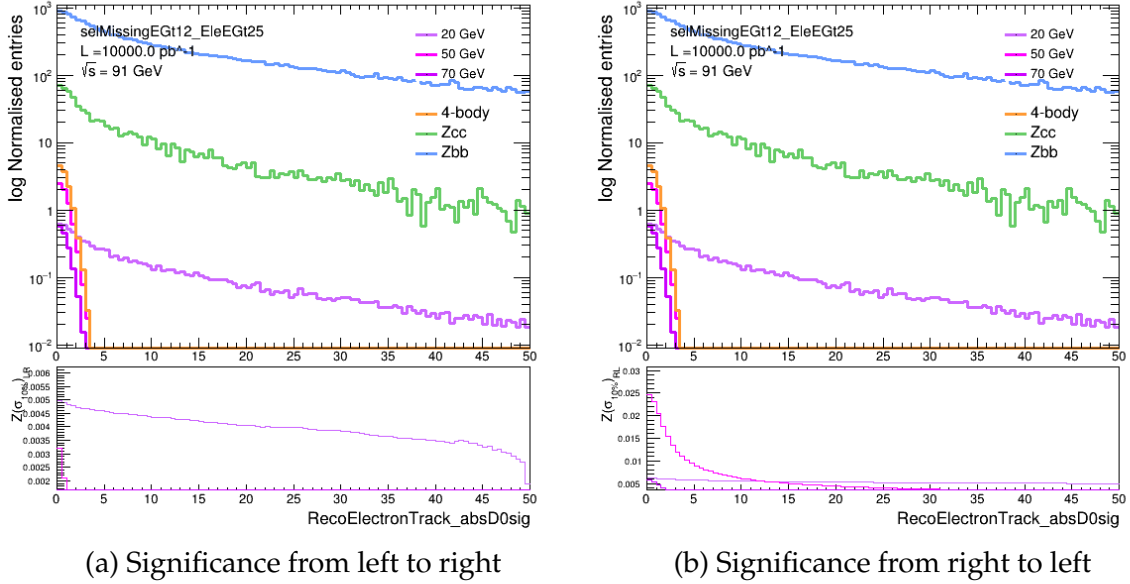


Figure 9 Comparison of significance distribution depending on the direction of the computation.

These show the  $\sigma_{d_0}$  distributions for the signal and background samples, with the significance computed from left to right (a) and right to left (b). If one wishes to focus on the 20 GeV signal, it seems natural to apply a cut at  $\sigma_{d_0} > 5$  in order to remove most of the background around 0. In that case, computing the cumulated

significance from left to right means that at each histogram bin, we compute how much significance remains if we were to select the data above some threshold. In the other case, if one wants to focus on the 50, 70 GeV signals (pink and dark purple), one would want to select only the events below a given threshold, say  $\sigma_{d_0} < 5$ . Then, the cumulated significance should be computed from right to left for the similar reasons as explained above.

### 4.1.3 Discriminating variables

In order to determine the appropriate selections to apply to enhance signal sensitivity, we have selected several variables with potential to show a good discrimination between the signal and the background presented in section 3.4.

The neutrino from the Z-boson decay in the signal final state, as well as potential subsequent neutrinos in the jets result in missing energy when these fail to be reconstructed by the detector — which happens almost all the time due to their feebly interacting nature. As the FCC-ee is a lepton collider, the total missing energy in the x,y and z directions can be studied. Since at least one neutrino originates from a 2-body decay where the HNL mass is fixed (by construction), our signal will typically contain a high missing energy compared to backgrounds such as Z to bb/cc. Figure [10] shows the distribution of the missing energy for three HNLs signals of masses 20, 50 and 70 GeV, with the previously introduced backgrounds and no event selection. From the distributions, one can tell that the signal for 20 GeV HNLs has



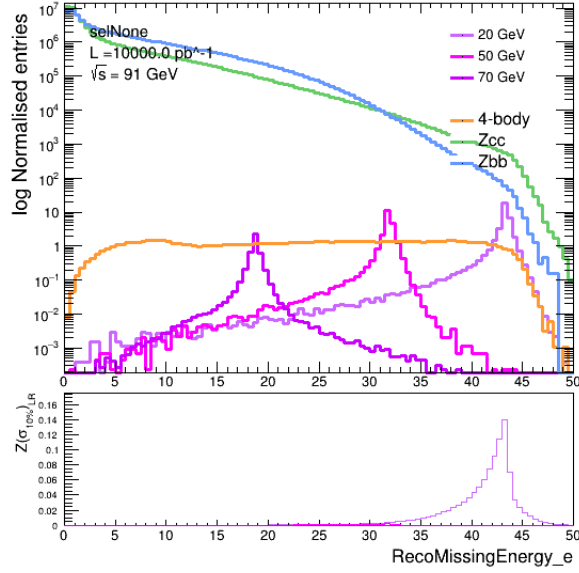


Figure 10 Reconstructed missing energy for three HNLs signals (upper legend) and three backgrounds (lower legend). No event selection applied. The lower part of the plot shows the significance computed according to equation [16].

the most significance for missing energy ( $\cancel{p}$ )  $> 40$  GeV, however this would remove most of the high HNL mass signal too. In order to preserve as much signal as possible, while removing the most background,  $\cancel{p} > 12$  GeV is picked as a first selection.

Keeping the same idea of high energy particles produced in decays, the lepton ( $e^+/e^-$ ) produced in the HNL decay along with two jets will typically have a high energy too, while the leptons produced in jets will typically have low energies. Figure [11] shows the energy distribution of the leading energy electron in each event for signals and backgrounds. From the distributions, it is clear that picking events with high leading electron energy will be a powerful selection to remove background while preserving most of the signal. In this analysis, different selections have been

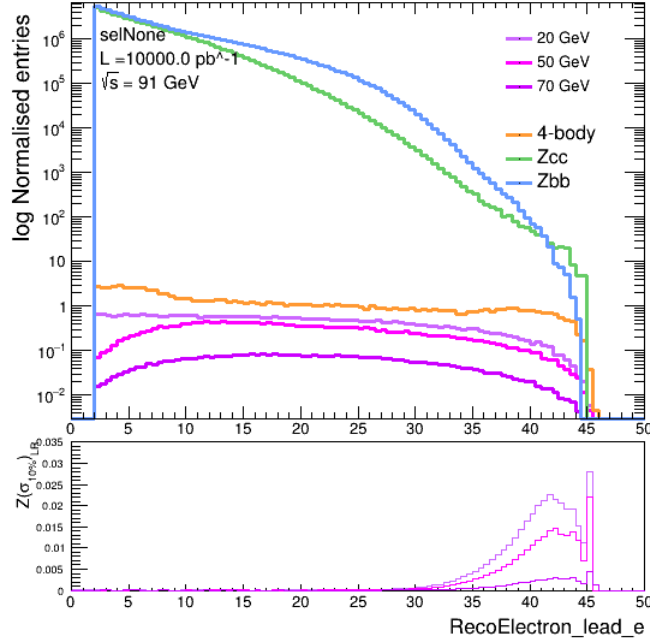


Figure 11 Leading electron energy for three HNLs signals (upper legend) and three backgrounds (lower legend). No event selection applied. The lower part of the plot shows the significance computed according to equation [16].

applied on the electron energy, namely  $E_{e^-} > 25, 30$ , and  $35$  GeV in order to investigate the balance between preserving more signal events with more permissive selections and removing most background with more aggressive ones.

Next, we take a look at different angular distributions which will also prove to be powerful discriminating variables. The angular separation between the two jets can also be a strong discriminating variable, as the  $Zbb$  and  $Zcc$  backgrounds will produce a good amount of back-to-back jets. On the other hand, signal jets from the decaying HNL will generally not be produced back-to-back because of the  $W$ -boson being off-shell. Figure [12] shows the angular distributions computed in two

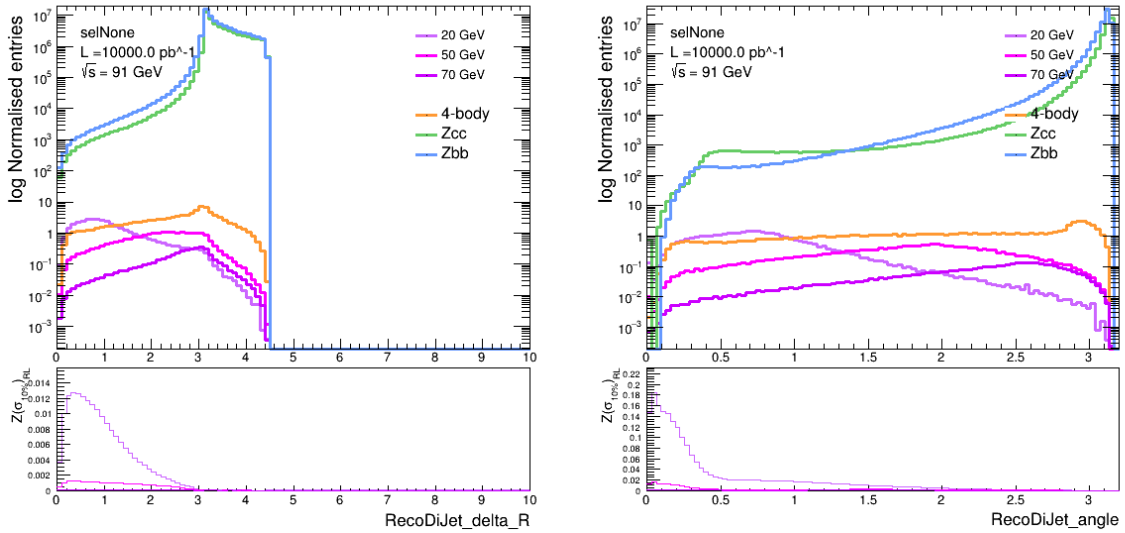
different ways. Figure [12a] shows the angular distance in the detector frame, defined as

$$\Delta R = \sqrt{\Delta\phi^2 + \Delta\eta^2} \quad (17)$$

where  $\Delta\phi$  is the distance in the azimuthal plane around the beam axis, and  $\Delta\eta$  is the difference in pseudorapidity, which is equivalent to a Lorentz-invariant angle in the orbital plane. In figure [12b] instead, the three-dimensional angle  $\Psi$  between the jets is computed according to

$$\Psi = \cos^{-1} \left( \frac{j_1 \cdot j_2}{|j_1||j_2|} \right) \quad (18)$$

Where  $j_i$  are defined as the jets 4-vectors.



(a)  $\Delta R$  between the two jets, as defined in equation [17].

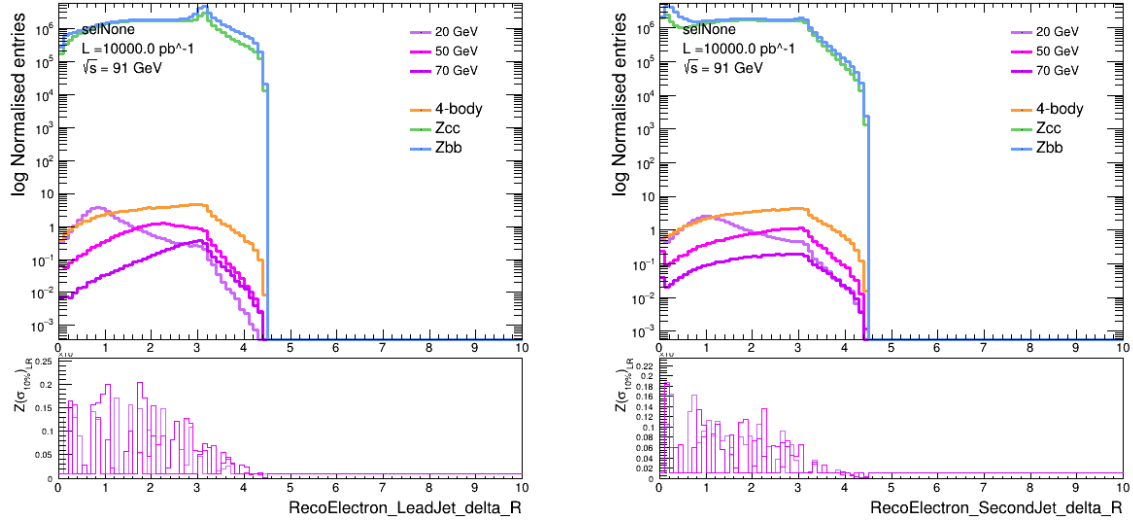
(b) 3D angle between the two jets, as defined in equation [18].

Figure 12 Distributions of angular difference between the two jets for signal and background samples.

These two variables are highly correlated — as they almost correspond to the same angle — , so we will only pick the one with the most discriminating power. In this case, in order to remove back-to-back jets corresponding to the backgrounds, we pick the 3D angle  $\Psi < 2.4$ .

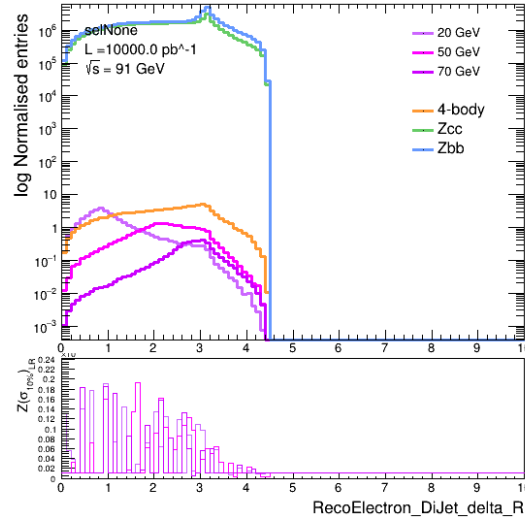
In addition, the  $\Delta R$  between the di-jet four-vector and the lepton, as well as the  $\Delta R$  between the leading/second leading jet (in energy) and the lepton are considered. These distributions are shown in figure [13]. The significance distributions are hard to interpret because of the presence of divergences in the significance formula given in equation [16], when very large backgrounds are present. Therefore, we will need to apply some selections before going back to these angular distributions, such that the amount of background is lowered and the divergences start to disappear, this process is described in section 4.1.4.

The last angular variable to consider is the angle between the leading electron and the missing momentum, shown in figure [14]. Indeed, since the leading electron and the neutrino in the signal are both produced from subsequent decays, while the ones present in the background are more random (as they appear via gluon radiation mostly), the angle between the two could be a good discrimination variable. From the distribution, it is clear that selecting events with  $\Theta < -0.5$  would constitute a good discrimination variable.



(a)  $\Delta R$  between leading jet and electron, no selection applied.

(b)  $\Delta R$  between second jet and electron, no selection applied.



(c)  $\Delta R$  between the di-jet and electron, no selection applied.

Figure 13  $\Delta R$  distributions for several variables for signal and background samples. The behaviour of the significance is due to the presence of divergences in the formula given in equation [16], when very large backgrounds are involved.

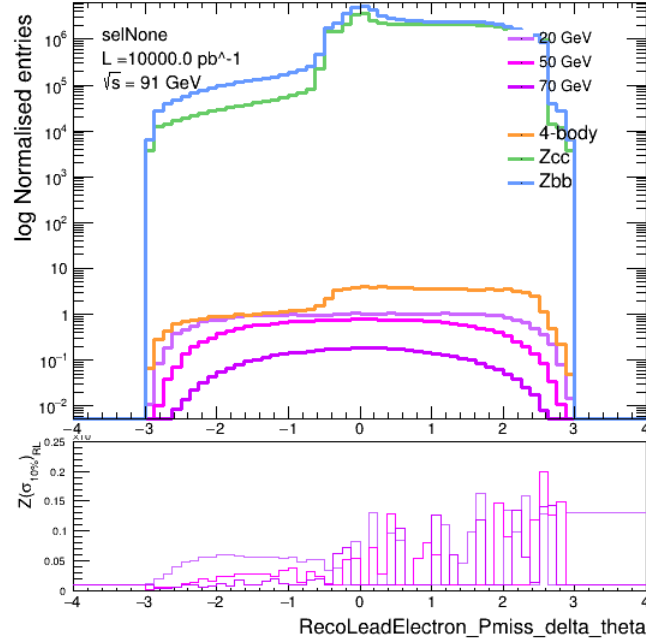


Figure 14  $\Theta$  angle between leading electron and missing momentum. No selection is applied.

The final variable to consider is the electron transverse impact parameter  $d_0$ . This variable represents the shortest distance in the transverse plane between the trajectory of a particle track and the reconstructed primary vertex (ref d0). Consequently, long-lived particles will typically have larger  $d_0$  values than short-lived particles. A standard way of measuring  $d_0$  is through its significance  $\sigma_{d_0}$ , defined as the impact parameter divided by its estimated error (ref d0). This analysis typically focuses on prompt (i.e short-lived) HNLs. However, when the mass approaches lower values ( $\approx 20$  GeV), the lifetime increases, which has a direct impact on  $\sigma_{d_0}$ . Figure [15] shows the distribution of the electron impact parameter for signal and background. From the distribution, we can see a clear difference between low and high HNL masses. Consequently, one could split the sensitivity analysis into long/short

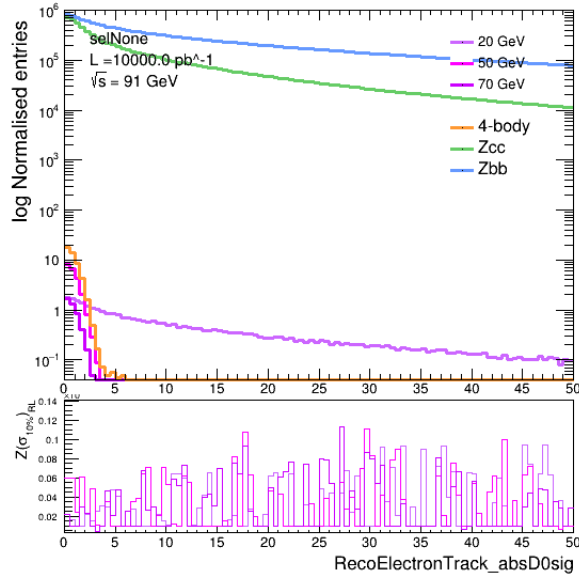


Figure 15  $\sigma_{d_0}$  distribution for the electron tracks. No selection is applied.

lived studies, by picking e.g  $\sigma_{d_0} > 5$  for long lived HNLs.

#### 4.1.4 Event selection

Now that the variables with good discrimination power have been identified, we need to check how the distributions evolve after each subsequent selection. Indeed, these variables could — probably — be correlated, and not maintain their discrimination power after each selection. In the following, only the variables which are chosen for selection are displayed, the other variables are displayed in the [Appendix C](#) for each subsequent selection.

As a first selection, missing energy (10)  $\cancel{p} > 12$  GeV is required. Figure [16] shows the leading electron energy after this selection. From the energy distribution

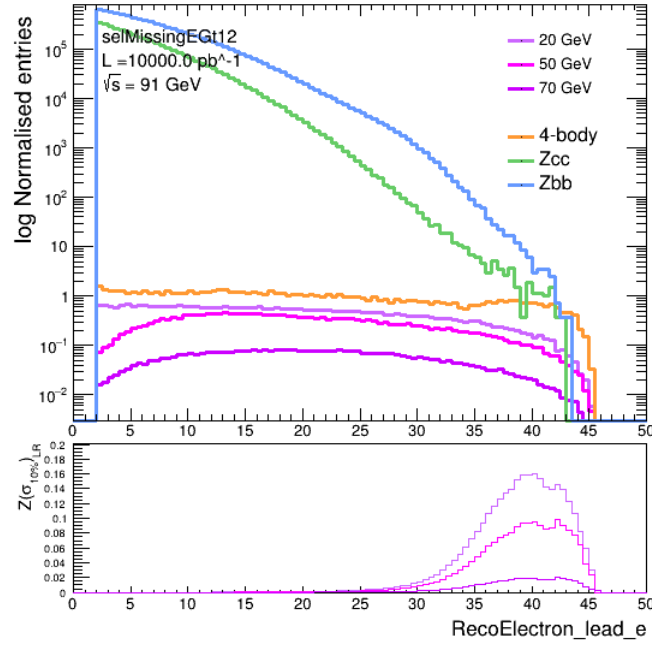


Figure 16 Leading electron energy after  $p_T > 12$  GeV is applied

in figure [16], the next selection that we require is  $E_{e^-} > 35$  GeV. The distributions for the three-dimensional angle  $\Psi$  and the  $\Delta R$  between the two jets after this selection are displayed in figure [17]. One variable worth mentioning at this point is the angle  $\Theta$  between leading electron and missing momentum. From its distribution shown in figure [18], we can see that the discrimination power present in figure [14] is now gone, as it probably came from lower energy electrons.

Nevertheless, in order to remove as much background as possible, we next require the  $\Psi < 2.4$  as the following selection. As mentioned in section 4.2.2,  $\Psi$  and  $\Delta R$  are closely related. Thus, only one selection will be applied. Finally, figure [19] shows the distribution of  $\Delta R$  between the leading electron and the di-jet system,



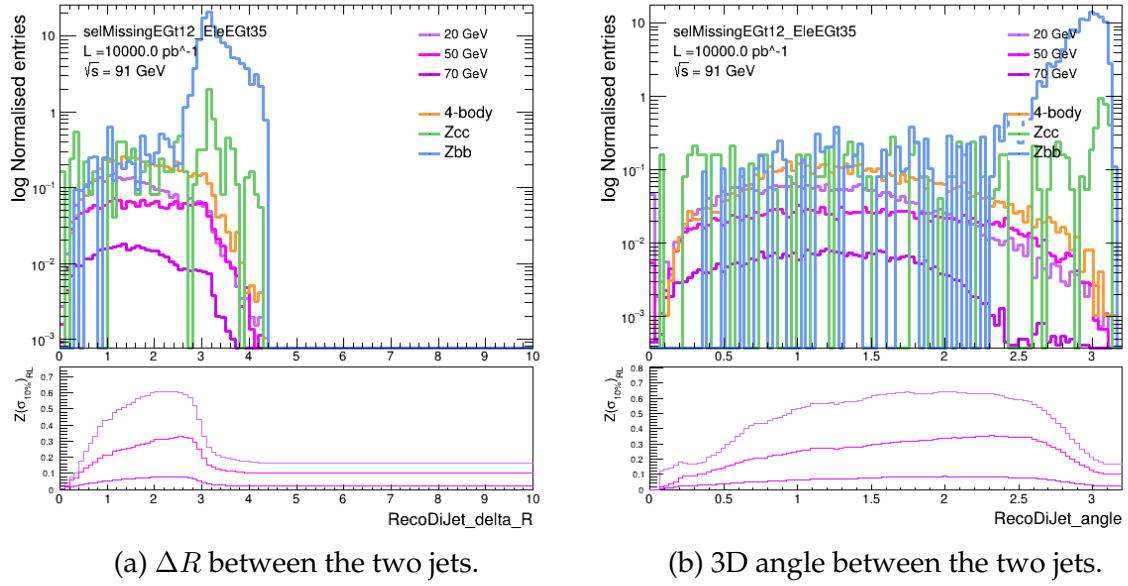


Figure 17 Distributions of angular difference between the two jets with selection  $\cancel{E} > 12$  &  $E_{e^-} > 35$  [GeV].

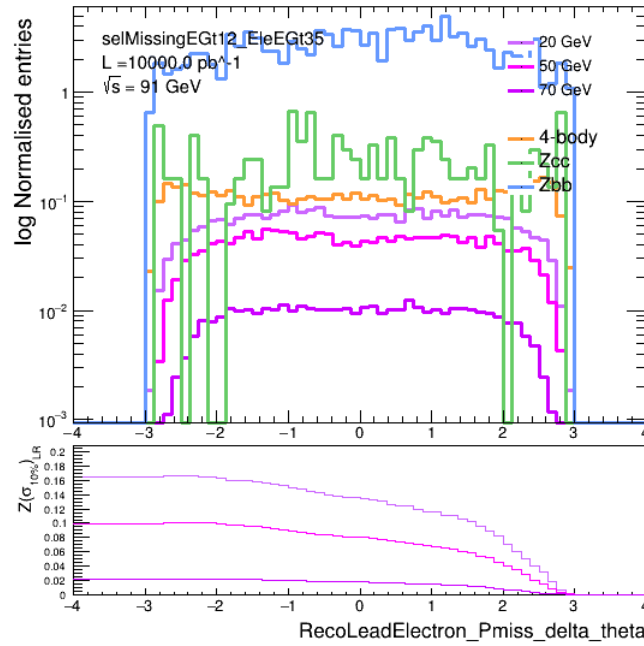


Figure 18  $\Theta$  angle between leading electron and missing momentum after  $E_{e^-} > 35$  is applied.

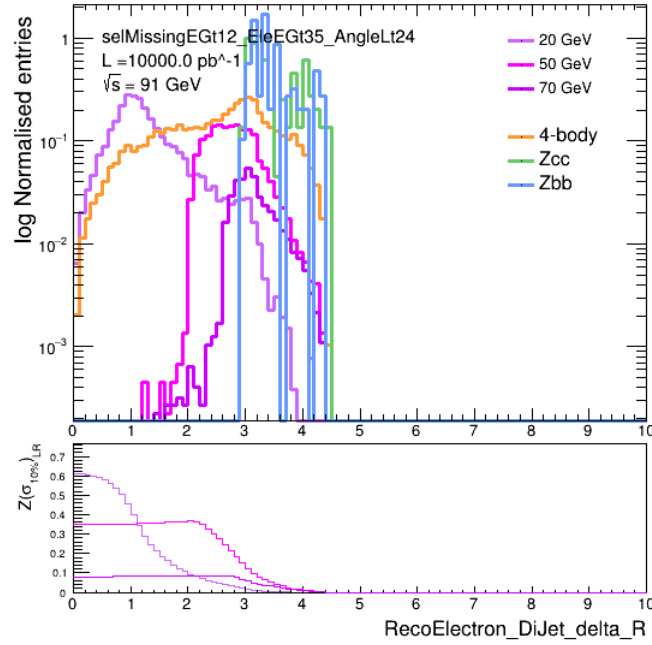


Figure 19  $\Delta R$  between electron and di-jet after selections  $\cancel{E} > 12$  &  $E_{e^-} > 35$  & 3D angle  $< 2.4$  are applied

with the Z to bb/cc background concentrated at high values. Consequently, the last selection consists of picking  $\Delta R < 3$ . A summary of the various event selection is given in table [3]. Table [4] shows the remaining number of generated events after each selection.

Variable	Selection
Missing Energy	$\cancel{E} > 12$ GeV
Electron Energy	$E_{e^-} > 35$ GeV
3D Di-jet Angle	$\Psi < 2.4$
Di-jet - Electron $\Delta R$	$\Delta R < 3$

TABLE 3 Summary table of the event selections.

Selection	20 GeV	50 GeV	70 GeV	4-body	$Z \rightarrow cc$	$Z \rightarrow bb$
No selection	$10^5$	$10^5$	$10^5$	$10^5$	$4.9 \times 10^8$	$4.4 \times 10^8$
$\cancel{E} > 12$	$9.9 \times 10^4$	$9.9 \times 10^4$	$9.9 \times 10^4$	$7.8 \times 10^4$	$3.3 \times 10^7$	$5.6 \times 10^7$
$\cancel{E} > 12 \ \& \ E_{e^-} > 35$	8079	8090	8541	5206	101	817
$\cancel{E} > 12 \ \& \ E_{e^-} > 35$ $\ \& \ \Psi < 2.4$	7780	7290	8333	4853	60	46
$\cancel{E} > 12 \ \& \ E_{e^-} > 35$ $\ \& \ \Psi < 2.4 \ \& \ \Delta R < 3$	7478	5035	3017	3184	2	1

TABLE 4 Summary table of the raw number of events after each subsequent selection.

From table [4], the selection on leading electron energy is highly effective for the hadronic  $Z$  decays. Furthermore, after the final selection on the  $\Delta R$  between the di-jet and the electron, almost all of the background from  $Z$  to quarks is removed (within statistical uncertainties), and the remaining background is due to the irreducible 4-body background. As stated before, at this point one could split the analysis into short/long lived HNLs by applying further selections on the HNL lifetime or on the  $\sigma_{d_0}$  for an increased discrimination.

#### 4.1.5 Results

A standard way of identifying new phenomena in particle physics is through what is referred to as "bump searches". It refers to the process of analyzing experimental data to look for an excess of events, or an unexpected peak or shift in the distribution of certain observable quantities. In this analysis, we focus on the HNL invariant mass as an observal quantity, defined in equation 19. The invariant mass of the signal can be reconstructed as the invariant mass of the di-jet and leading

electron four-vector.

$$m = \sqrt{E^2 - \sum_i p_i^2} \quad (19)$$

Figure [20] shows the invariant mass distribution for the three signals and backgrounds, along with the computed significance  $Z$  compared to the simplified significance defined as  $\frac{s}{\sqrt{s+b}}$ .

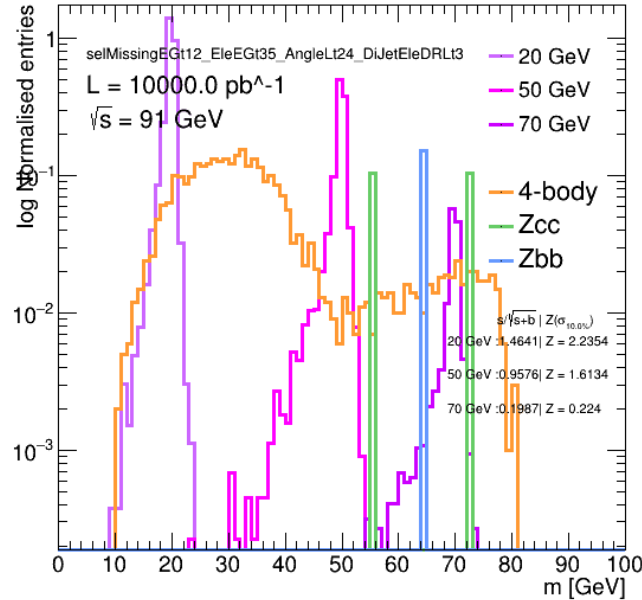


Figure 20 Invariant mass distributions for HNL masses of 20, 50 and 70 GeV and coupling  $V_{eN} = 10^{-3}$ ,  $L = 10\text{fb}^{-1}$ , with the backgrounds defined in section 3.4. Two significances are computed in the region around the mass peak, with  $Z$  defined as in equation [16]. Full event selection as defined in table [3] is applied.

As mentionned earlier, the event selection has been performed for masses of 20, 50 and 70 GeV, and a mixing angle of  $V_{eN} = 10^{-3}$ , with the purpose of enhancing signal significance by removing efficiently the background events while preserving

the signal as much as possible across HNL mass range. This selection can then be extended to a larger range of masses and couplings in order to obtain a contour plot, showing the exclusion power of this analysis. Figure [21] shows the significance computed for mass ranges of 10-80 GeV and couplings of  $|V_{eN}|^2 = 10^{-4} - 10^{-10}$ , for an integrated luminosity of  $10 \text{ fb}^{-1}$  and the target of the FCC-ee luminosity of  $150 \text{ ab}^{-1}$ , with the red line delimiting the  $Z = 2$  threshold.

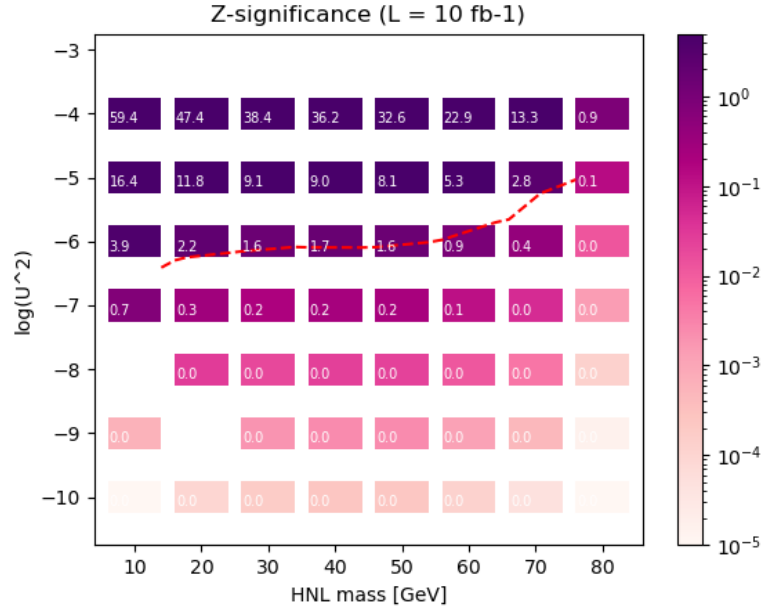
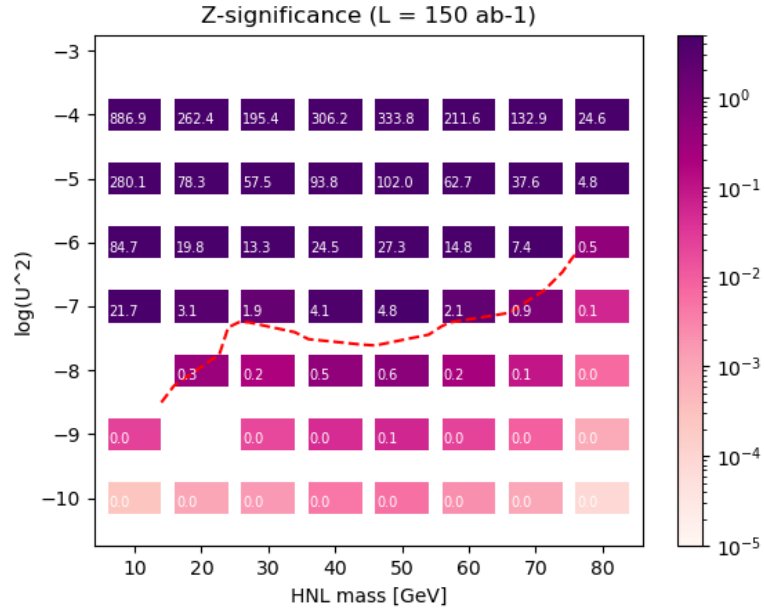
(a)  $L = 10 \text{ fb}^{-1}$ .(b)  $L = 150 \text{ ab}^{-1}$ 

Figure 21 Contour plots for various HNL masses and couplings. The red dashed line delimits the  $Z=2$  threshold, with  $Z$  being the significance as computed in 16.

From the contour plot, we can see that the  $Z=2$  threshold is attained for couplings below  $|V_{eN}|^2 = 10^{-7}$  for masses below 60 GeV. Higher masses have lower exclusion power, as the discrimination is less efficient when the HNL mass gets closer to the  $Z$  boson mass.

#### 4.1.6 Outlook

There can be several suggestions for a more complete continuation of this work. First and foremost, an extension of the background samples is necessary in order to reduce the uncertainties on the significance scaling, as well as the consideration of other background processes such as  $Z$  to light quarks, and  $Z$  to  $e^+e^-$ . This would also allow for more precise event selections to be applied, as once the background statistics is too low (see figure [19]), it becomes almost impossible to identify any type of trend or behaviour to pick a selection.

A more complete analysis would also include a thorough consideration of both statistical and systematic uncertainties. Eventually, as stated before, a study separating short from long-lived HNLs based on the lifetime,  $d_0$  impact parameter or even using timing information would without a doubt provide interesting results. Finally, the incorporation of more sophisticated tools to separate signal from background, such as Boosted Decision Trees (BDT) or the introduction of Deep Neural Networks could provide a powerful additional discriminant to enhance signal significance.

## 4.2 Dirac vs. Majorana discrimination

A logical way of pursuing this sensitivity study for the FCC-ee is the following : suppose that we have now discovered HNLs (the ones corresponding to our benchmark model), are we able to tell if these are Dirac or Majorana particles ? Determining this is equivalent to observing processes involving HNLs which show LNV properties. However, the direct way of observing LNV processes is through the detection of neutrinos (i.e. the detection of all the leptons in the event), which is not a possibility at the FCC-ee. Therefore one should use other metrics, such as asymmetries and angular distributions where the LNV nature of the processes can be identified.

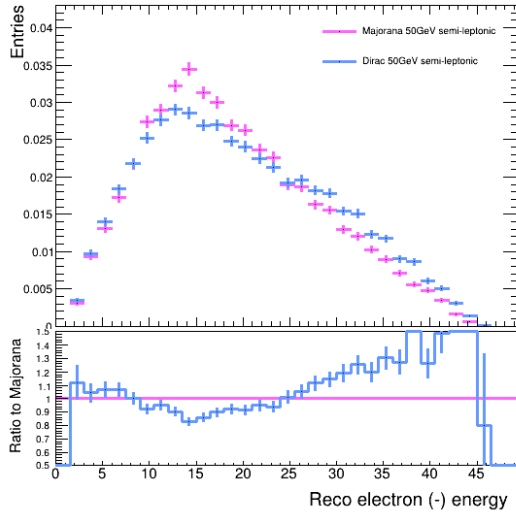
Similarly to the sensitivity analysis, the potential to distinguish the Dirac or Majorana nature of HNLs is explored in the semi-leptonic decay channels. A fully-leptonic analysis for the same masses (20, 50, 70 GeV) and coupling ( $|V_{eN}| = 10^{-3}$ ) already exists [37] and is the one which paved the way for this analysis. This part of the analysis is then the logical continuation of the fully-leptonic study, as the semi-leptonic decays of HNLs have about twice as large a branching ratio.



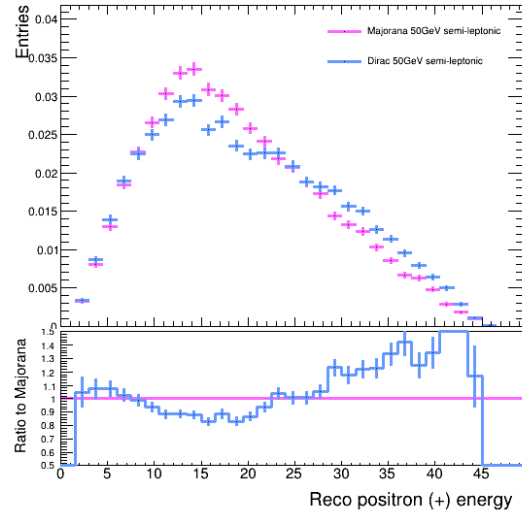
#### 4.2.1 Explored variables

The samples for this analysis were produced according to what is described in sections 3.1 and 3.3. All distributions are shown at reconstructed level, i.e. after the detector's response has been simulated.

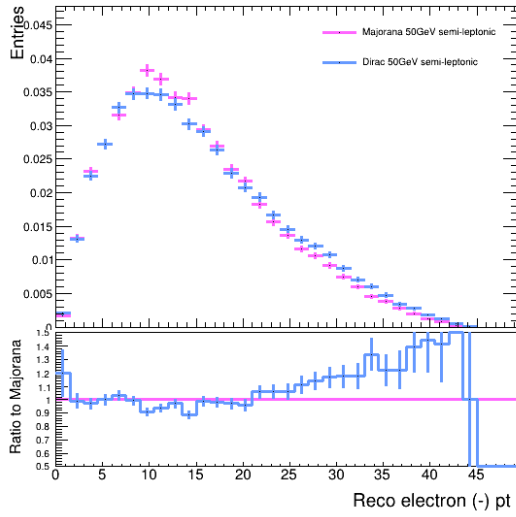
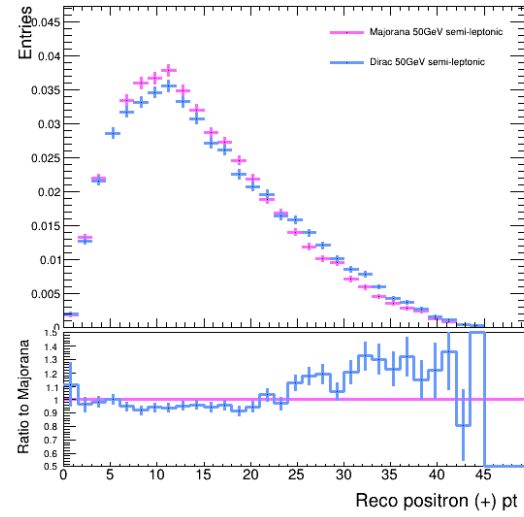
The kinematical variables distributions, namely  $p_T$ ,  $\eta$ ,  $\phi$ ,  $\theta$  and  $E$  of the leading energy electrons and positrons (assumed to be the one from the HNL decay) are displayed in figure [22]. Next, kinematics of jet-related variables have been explored. Leading and second-leading jet kinematical variables are shown in figure [23]. Figure [24] shows the kinematics of the Di-Jet system formed of the two leading jets four-vectors, and figure [25] shows the differences between the two leading jets. Finally, the angular difference in  $\theta$  between the reconstructed HNL, and the leading electron (positron), where the HNL is defined as two leading jets and an electron (positron), is shown in figure [26]. This variable is particularly interesting as it could capture a significant difference between Dirac and Majorana HNLs by indirectly measuring a forward-backward asymmetry due to the presence of parity violation in Dirac HNL decays, see [14] for more details.

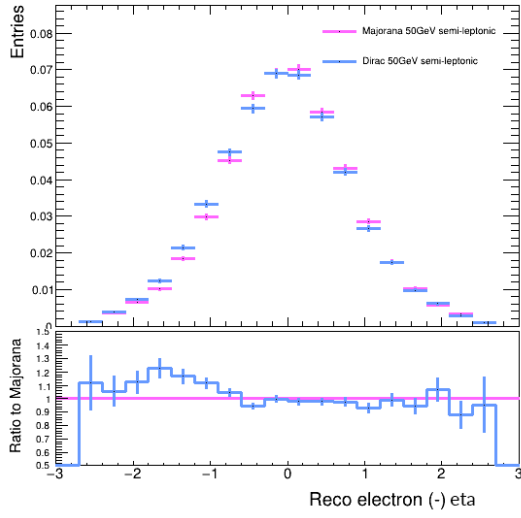
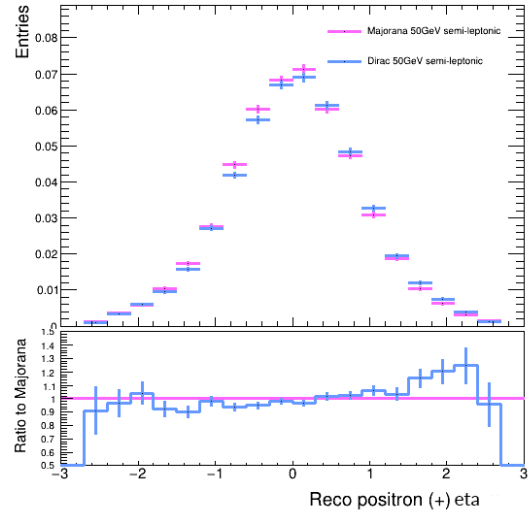
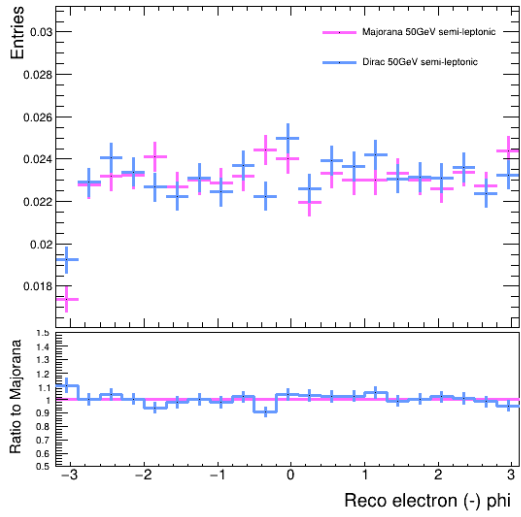
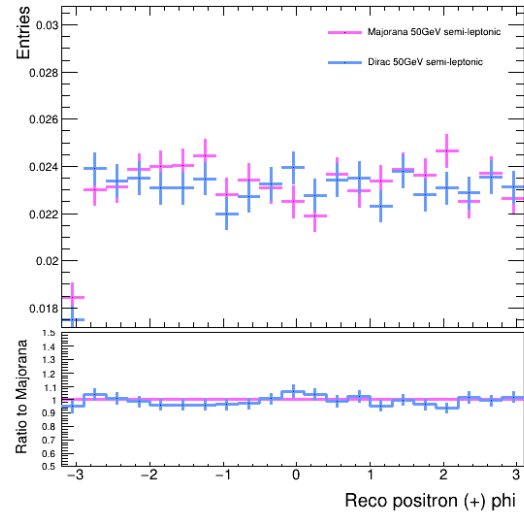


(a) Leading electron energy.



(b) Leading positron energy.

(c) Leading electron  $p_T$ .(d) Leading positron  $p_T$ .

(e) Leading electron  $\eta$ (f) Leading positron  $\eta$ (g) Leading electron  $\phi$ (h) Leading positron  $\phi$

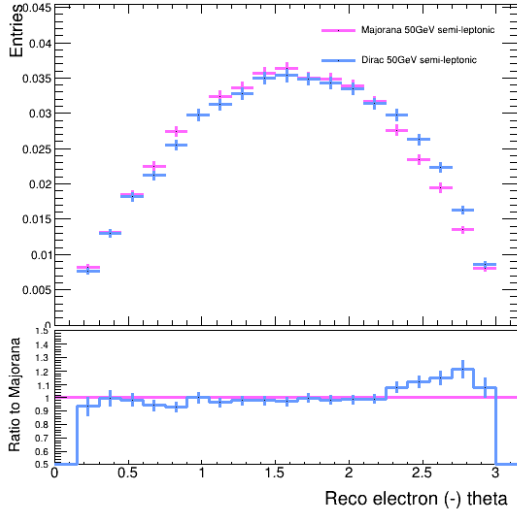
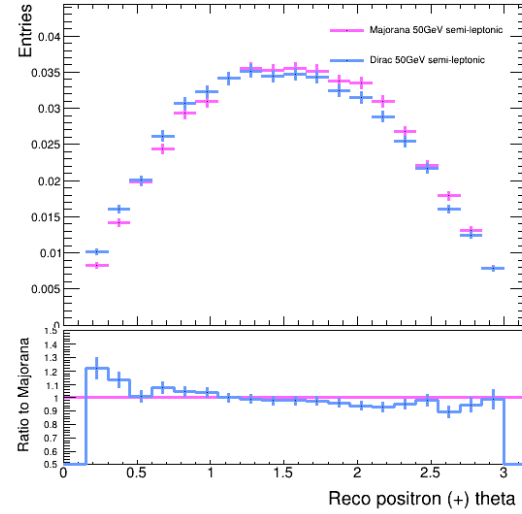
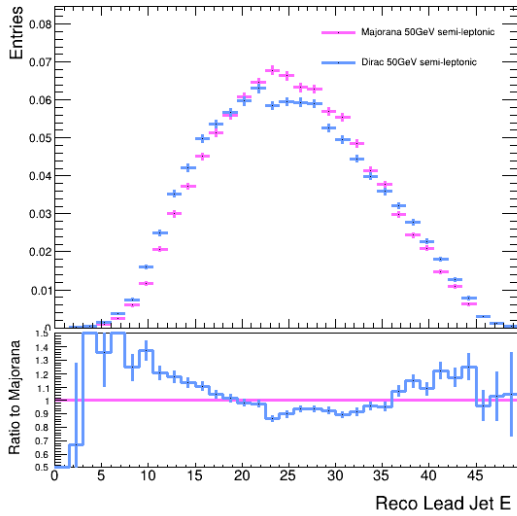
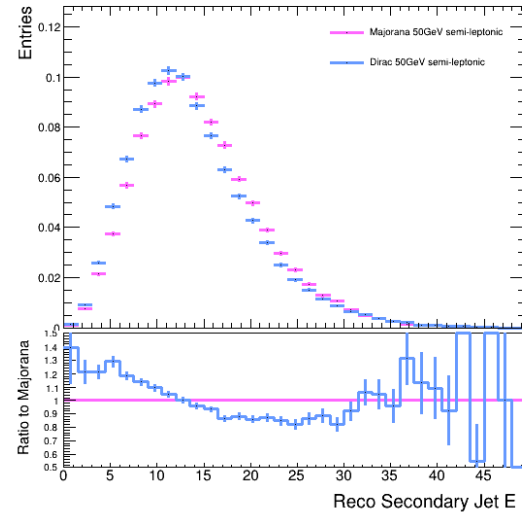
(i) Leading electron  $\theta$ (j) Leading positron  $\theta$ 

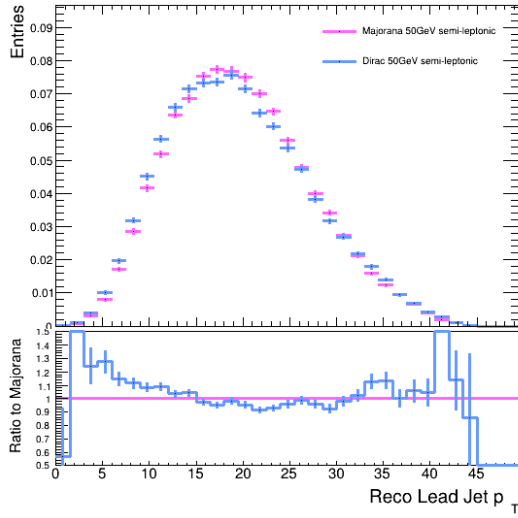
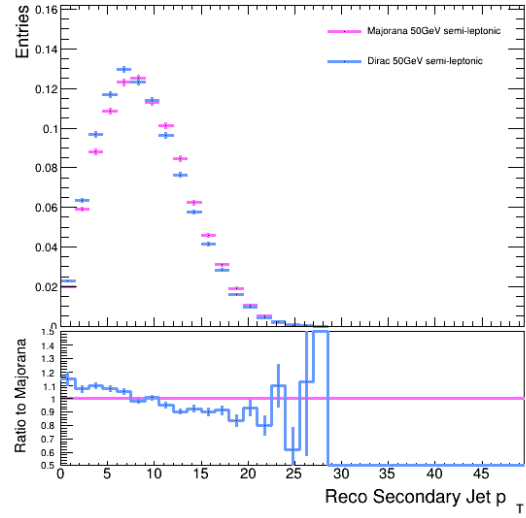
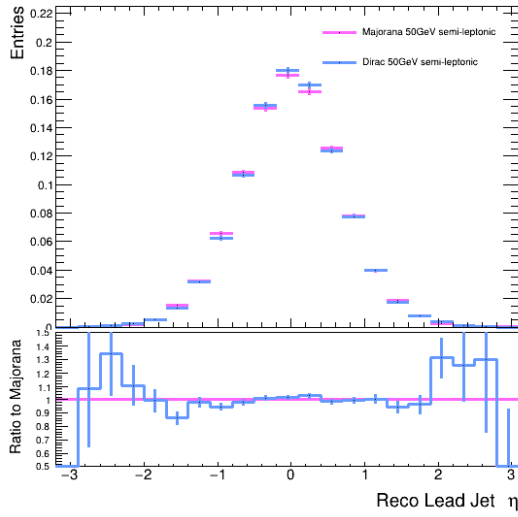
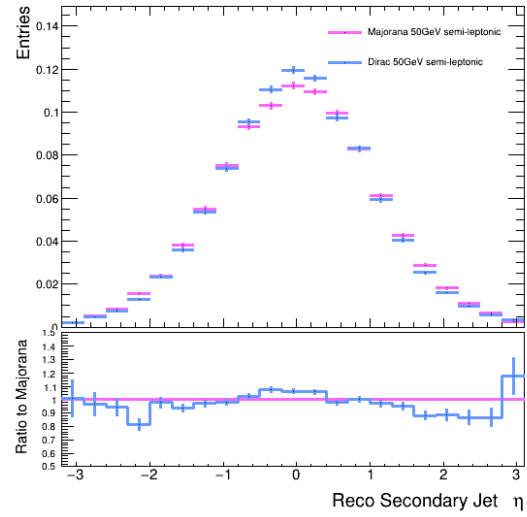
Figure 22  $e^-$  and  $e^+$  kinematical variables distributions for Dirac (blue) and Majorana (pink) HNLs with  $m_N = 50$  GeV, coupling  $|V_{eN}| = 10^{-3}$ .



(a) Leading jet energy.



(b) Second leading jet energy.

(c) Leading jet  $p_T$ .(d) Second-Leading jet  $p_T$ .(e) Leading jet  $\eta$ (f) Second leading jet  $\eta$

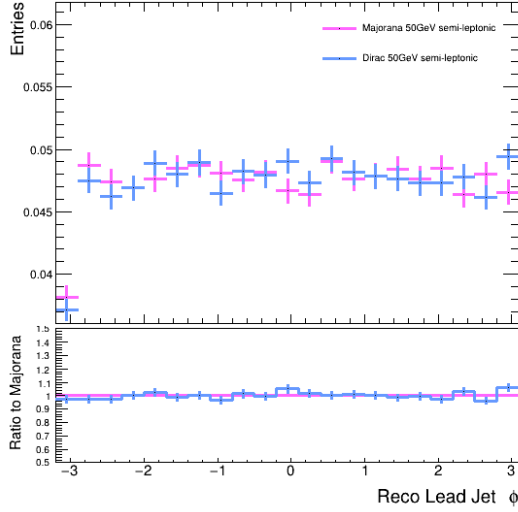
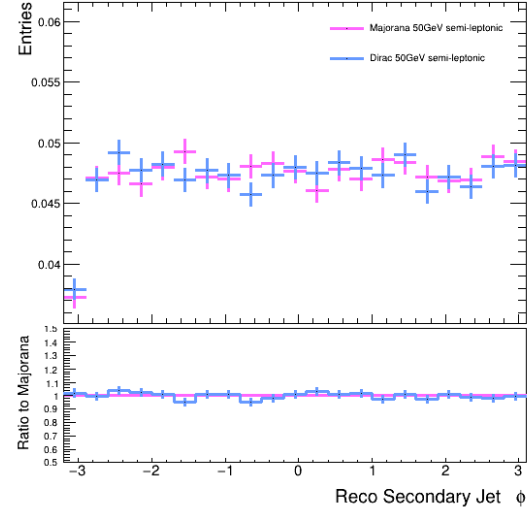
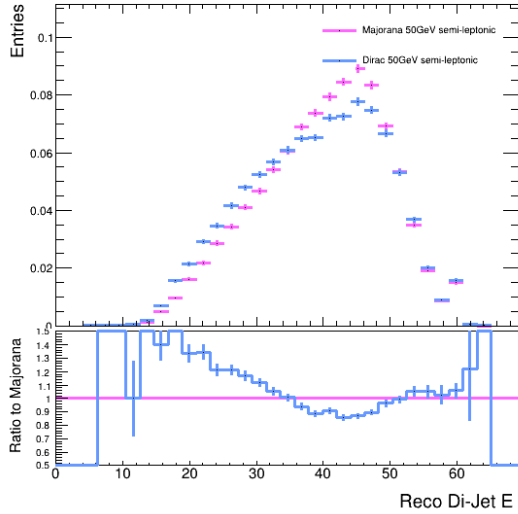
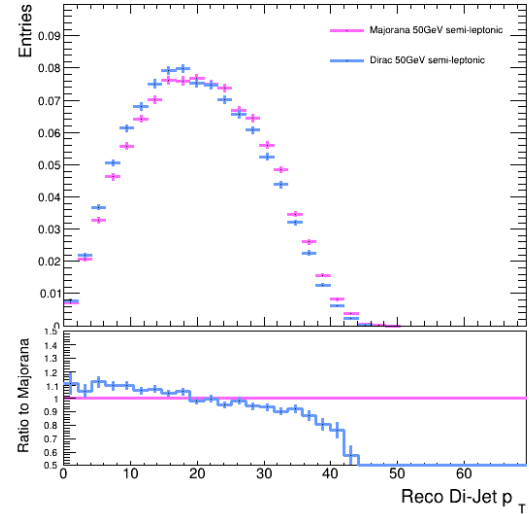
(g) Leading jet  $\phi$ (h) Second-leading jet  $\phi$ 

Figure 23 Leading and second leading jets kinematical variables distributions for Dirac (blue) and Majorana (pink) HNLs with  $m_N = 50$  GeV, coupling  $|V_{eN}| = 10^{-3}$ .



(a) Di-jet energy

(b) Di-jet  $p_T$ .

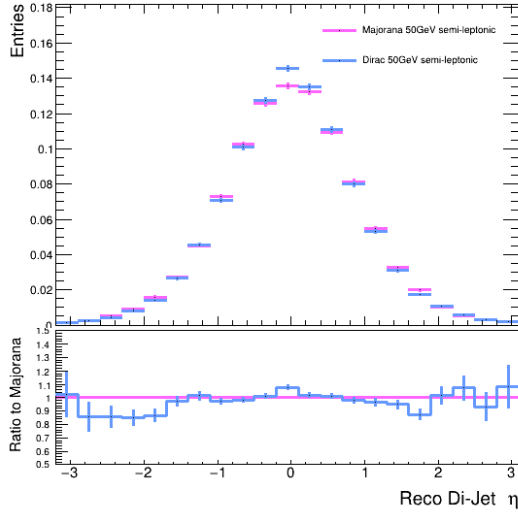
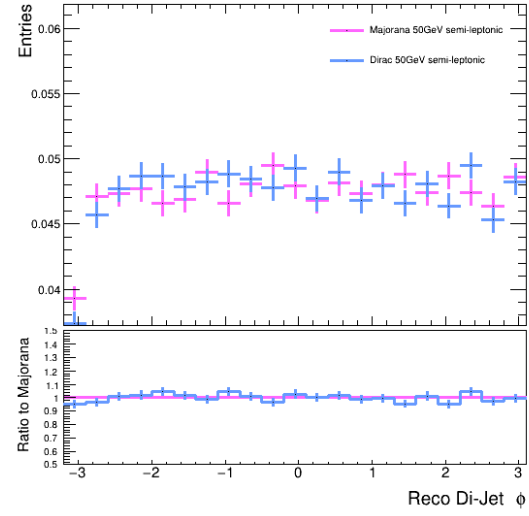
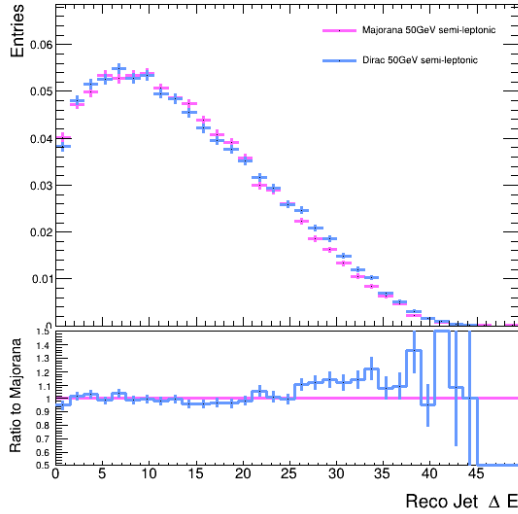
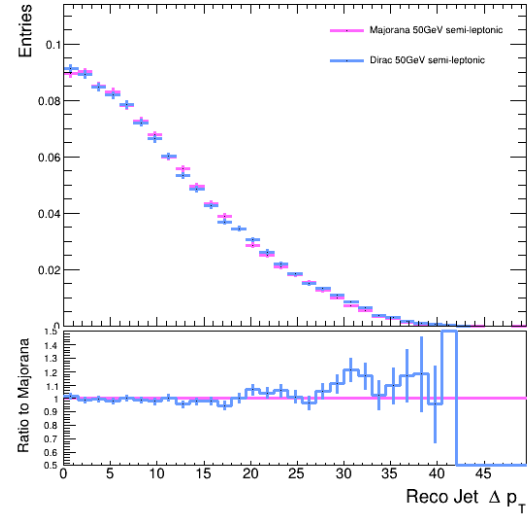
(c) Di-jet  $\eta$ .(d) Di-jet  $\phi$ .

Figure 24 Di-jet system kinematical variables distributions for Dirac (blue) and Majorana (pink) HNLs with  $m_N = 50$  GeV, coupling  $|V_{eN}| = 10^{-3}$ .

(a) Di-jet  $\Delta E$ (b) Di-jet  $\Delta p_T$ .

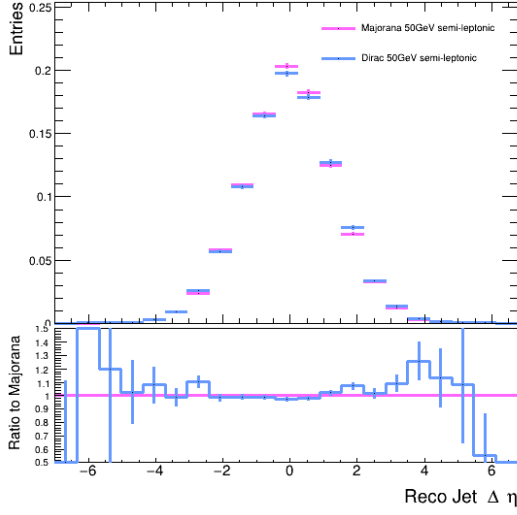
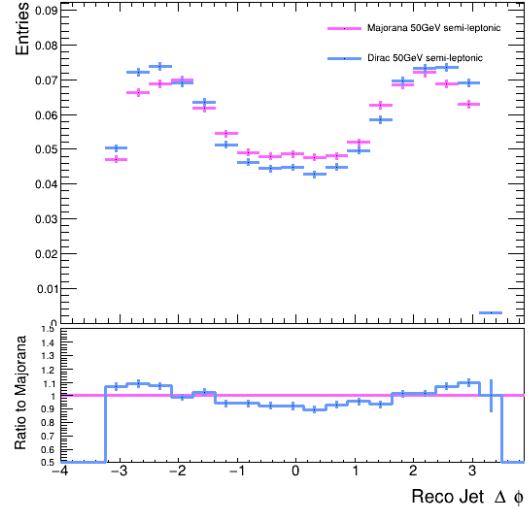
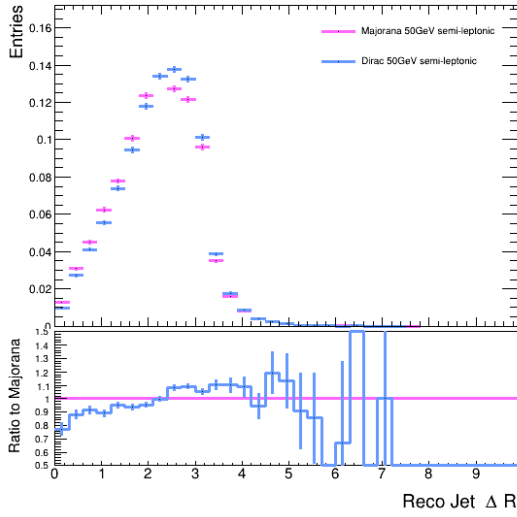
(c) Di-jet  $\Delta\eta$ .(d) Di-jet  $\Delta\phi$ .(e) Di-jet  $\Delta R$ .

Figure 25 Differences between leading and second leading jets for several kinematical variables for Dirac (blue) and Majorana (pink) HNLs with  $m_N = 50$  GeV, coupling  $|V_{eN}| = 10^{-3}$ .



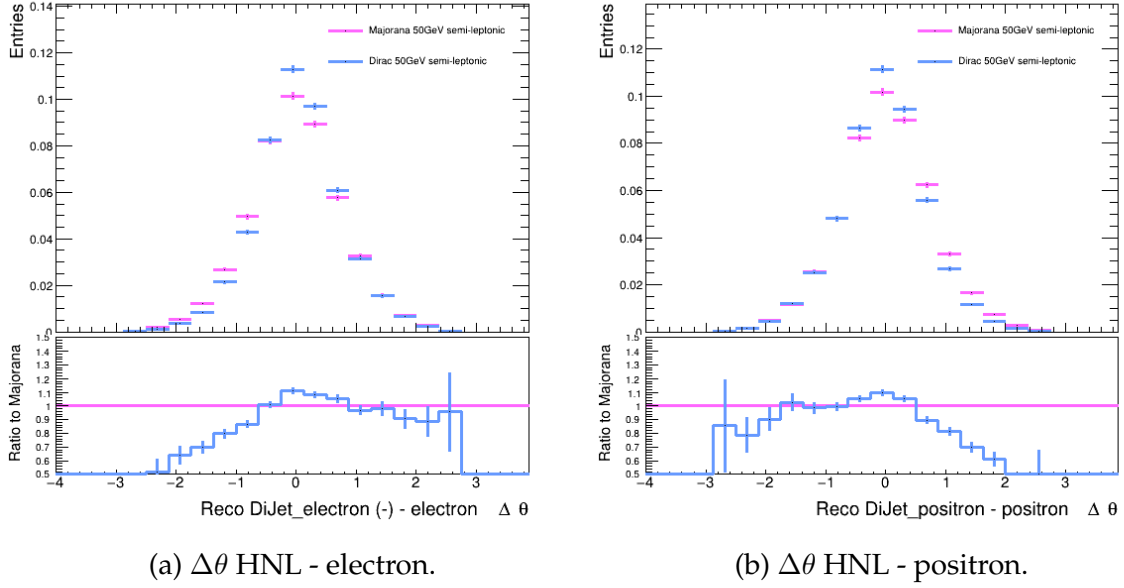
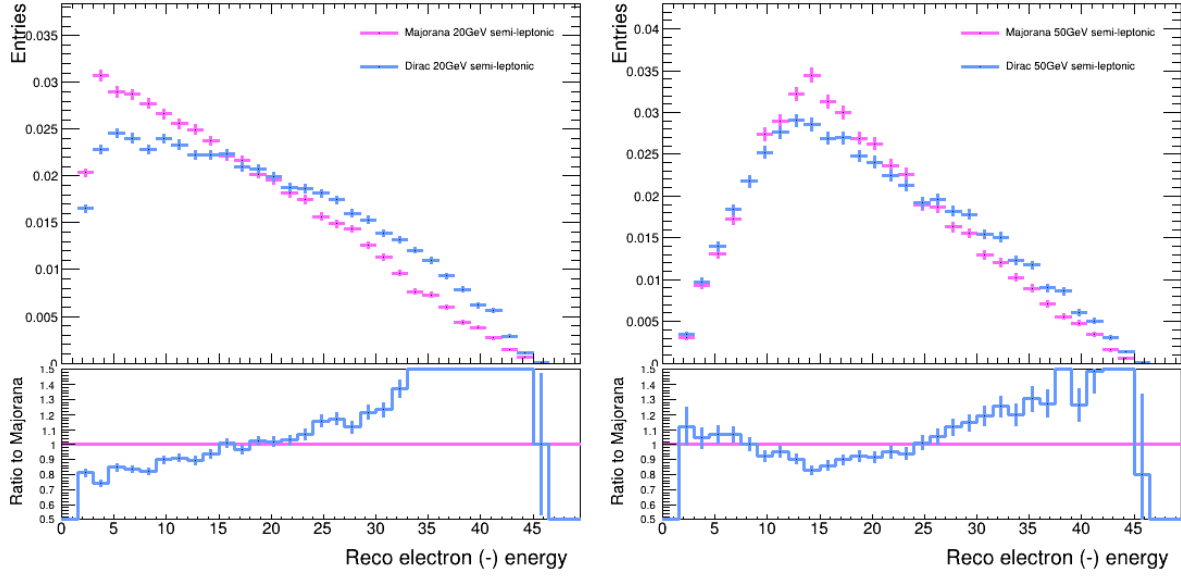


Figure 26  $\Delta\theta$  between the reconstructed HNL, built as the di-jet system with the leading lepton, for Dirac (blue) and Majorana (pink) HNLs with  $m_N = 50$  GeV, coupling  $|V_{eN}| = 10^{-3}$ .

#### 4.2.2 Discriminating variables

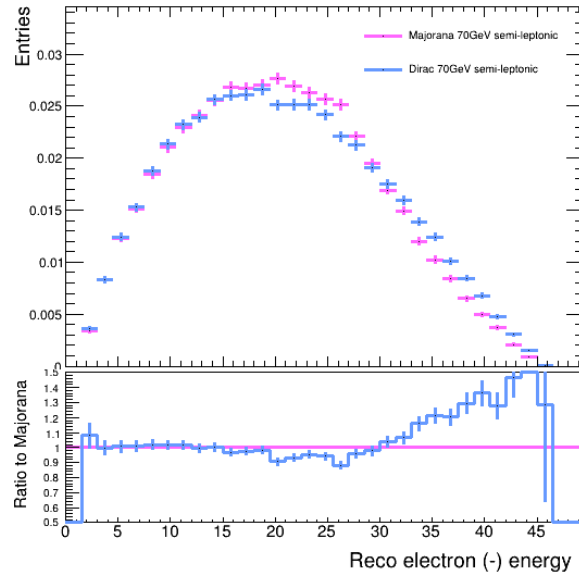
Most of the variables presented in the last section show some discrimination power between Dirac and Majorana, however these can be very small and will therefore be sensitive to the amount of statistics available. For HNL masses of 50 GeV, table [1] shows that for a coupling of  $V_{eN} = 10^{-3}$  about  $10^5$  events are expected, which coincides with the statistics in this analysis. However, as the mixing (mass) decreases (increases) fewer events are to be expected. Thus, it would be useful for a future study to estimate the expected number of events for pairs of mass/coupling which are able to generate neutrino masses in the eV scale. For this analysis, it is sufficient to keep in mind that the discrimination power is dependent on the amount of statistics available at the FCC-ee. Consequently, a summary of the variables sho-

wing the highest discrimination power between Dirac and Majorana is shown in figure [27] for HNL masses of  $m_N = 20, 50$  and  $70$  GeV with coupling  $V_{eN} = 10^{-3}$ .

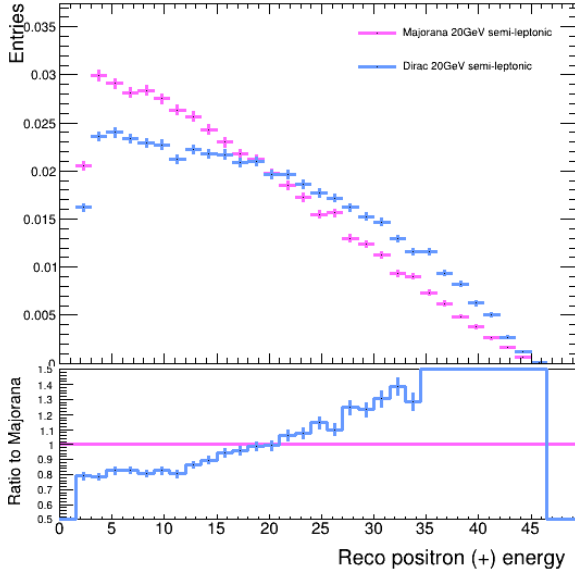
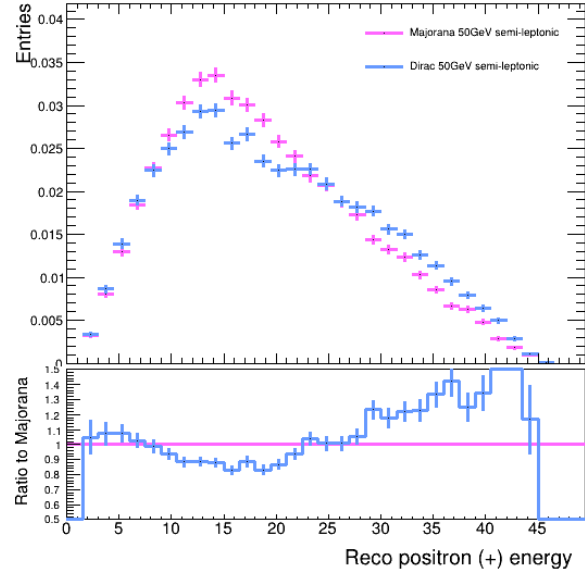
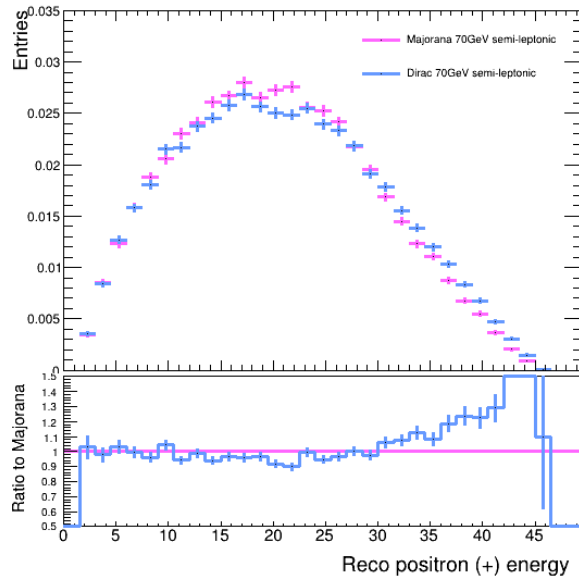


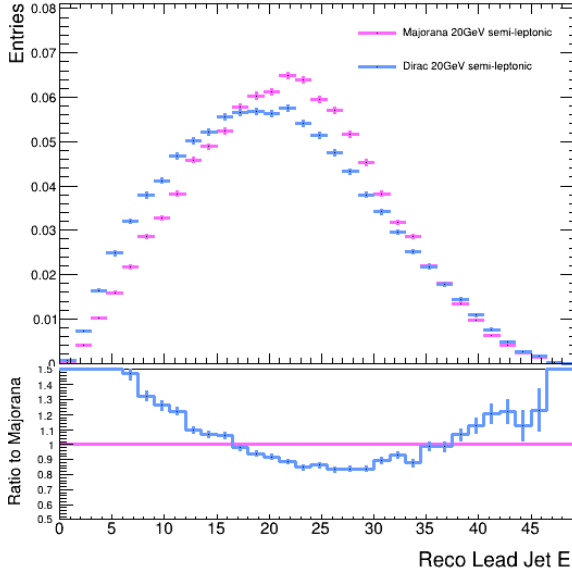
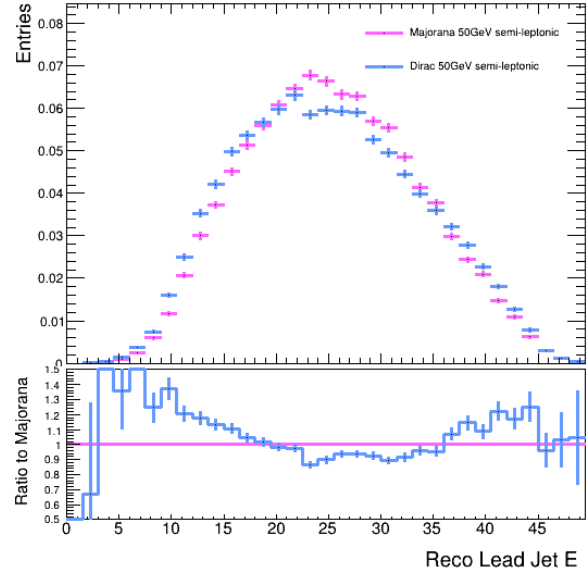
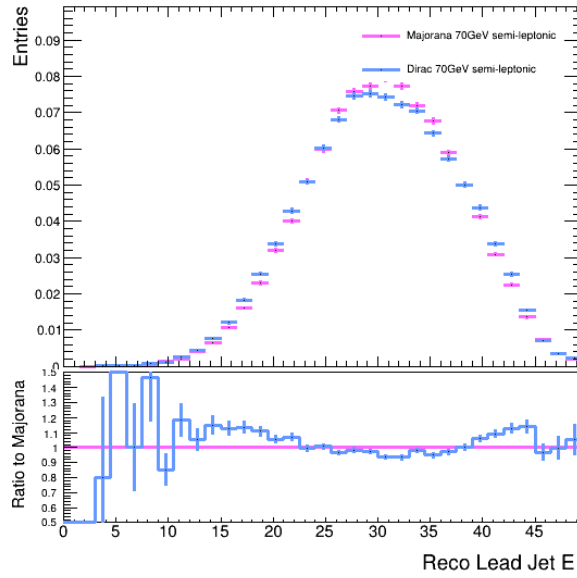
(a)  $e^-$  energy distribution,  $m_N = 20$  GeV.

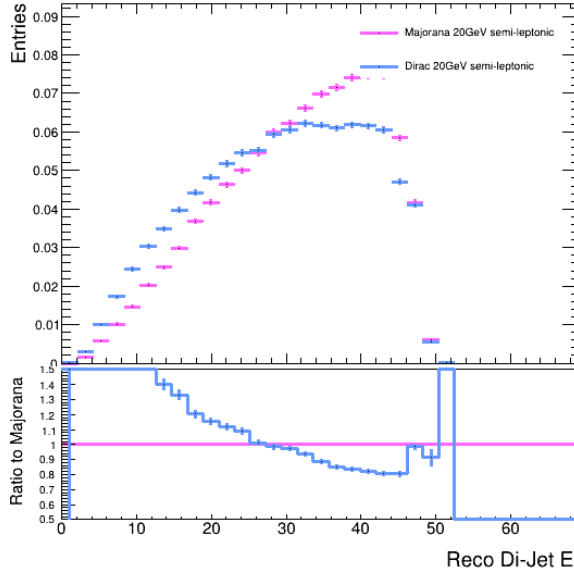
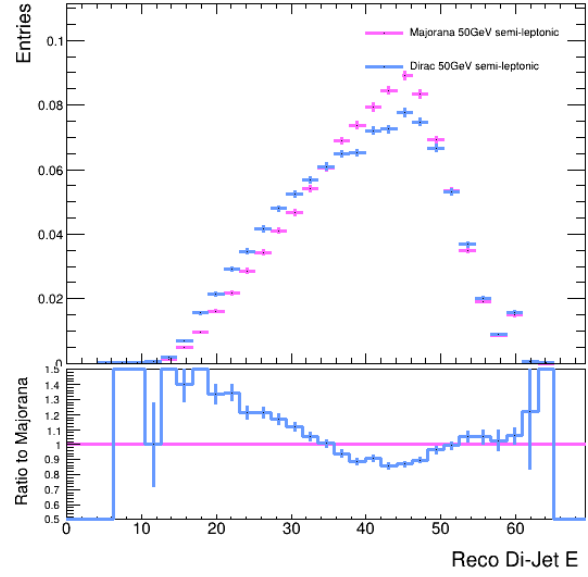
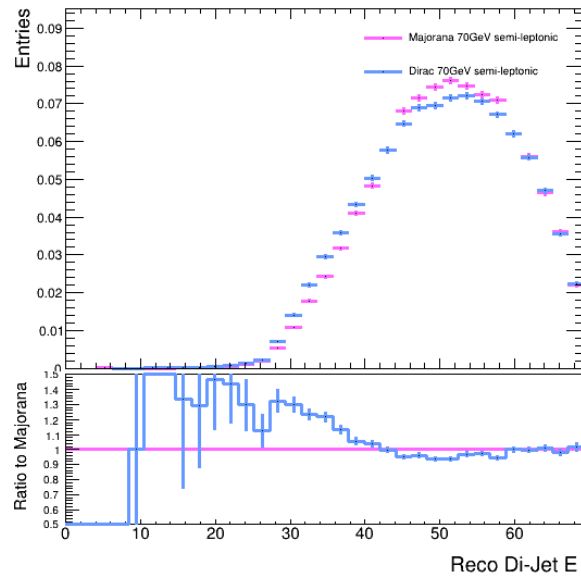
(b)  $e^-$  energy distribution,  $m_N = 50$  GeV.

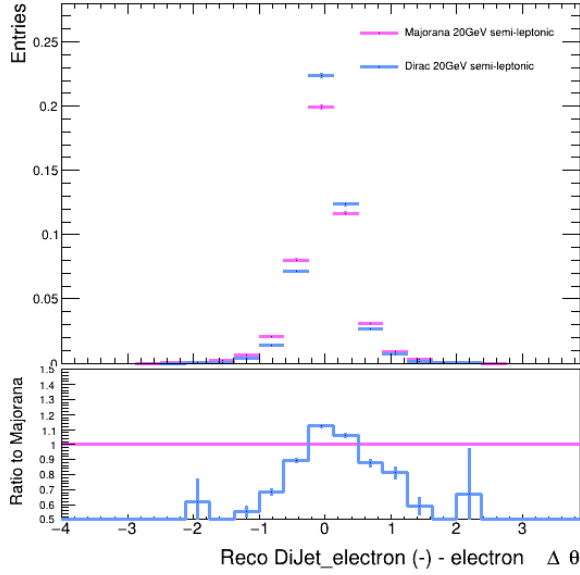
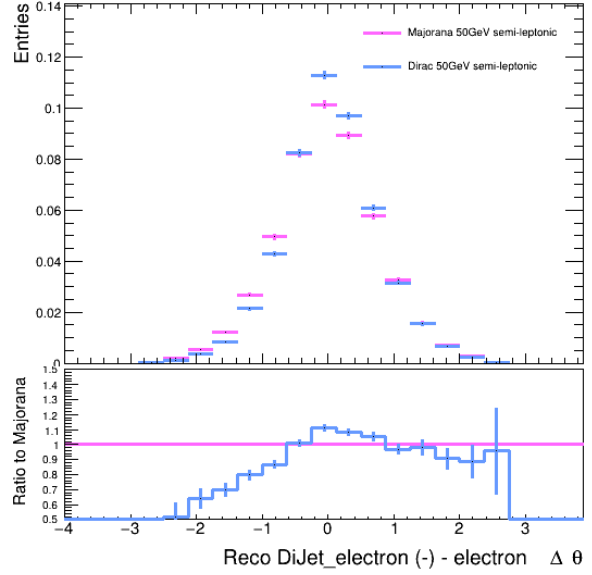
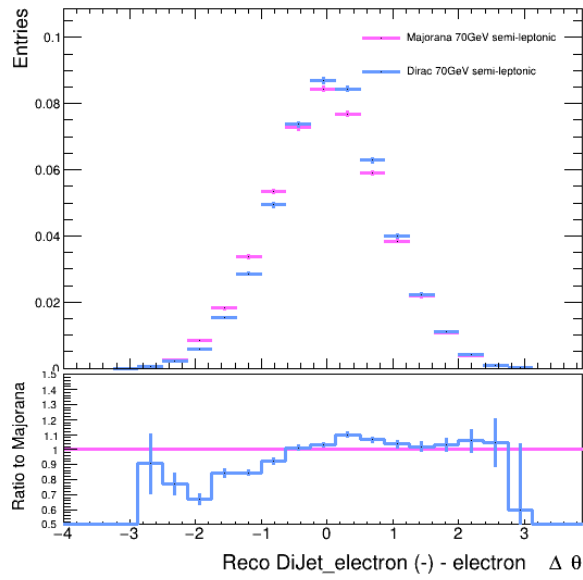


(c)  $e^-$  energy distribution,  $m_N = 70$  GeV.

(d)  $e^+$  energy distribution,  $m_N = 20$  GeV.(e)  $e^+$  energy distribution,  $m_N = 50$  GeV.(f)  $e^+$  energy distribution,  $m_N = 70$  GeV.

(g) Leading jet energy,  $m_N = 20$  GeV.(h) Leading jet energy,  $m_N = 50$  GeV.(i) Leading jet energy,  $m_N = 70$  GeV.

(j) Di-jet energy,  $m_N = 20$  GeV.(k) Di-jet energy,  $m_N = 50$  GeV.(l) Di-jet energy,  $m_N = 70$  GeV.

(m)  $\Delta\theta$  HNL -  $e^-$ ,  $m_N = 20$  GeV.(n)  $\Delta\theta$  HNL -  $e^-$ ,  $m_N = 50$  GeV.(o)  $\Delta\theta$  HNL -  $e^-$ ,  $m_N = 70$  GeV.

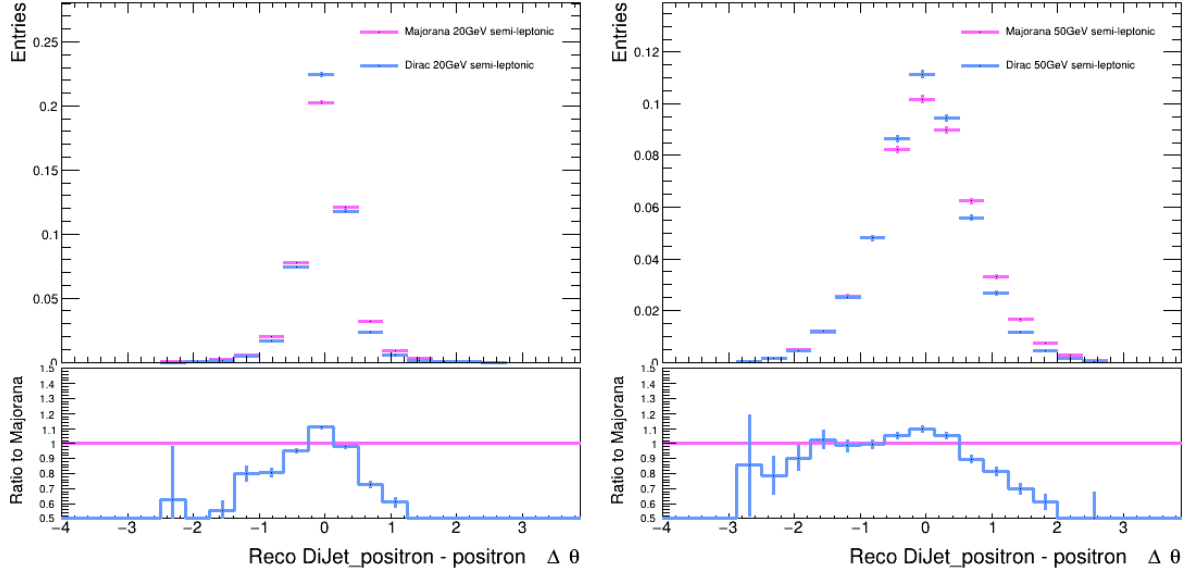
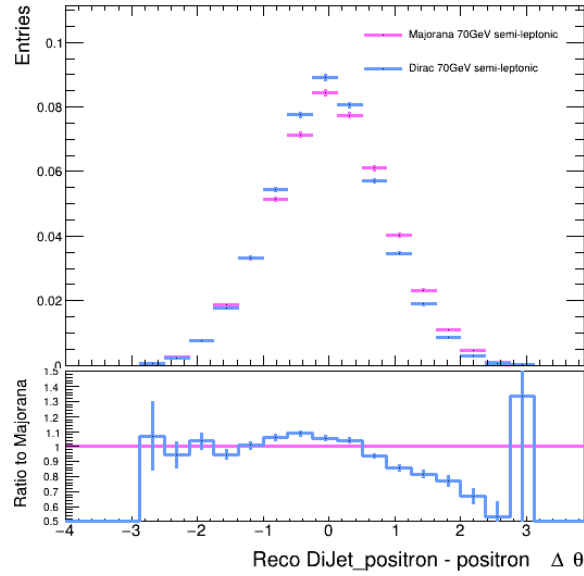
(p)  $\Delta\theta$  HNL -  $e^+$ ,  $m_N = 20$  GeV.(q)  $\Delta\theta$  HNL -  $e^+$ ,  $m_N = 50$  GeV.(r)  $\Delta\theta$  HNL -  $e^+$ ,  $m_N = 70$  GeV.

Figure 27 Distributions of the best discriminating variables for Dirac (blue) vs. Majorana (pink) HNLs with mass  $m_N = 20, 50$  and  $70$  GeV and coupling  $|V_{eN}| = 10^{-3}$ . The lower part of each plot shows the ratio between Dirac and Majorana.

From the distributions in the summary figure, it appears that the energy distribution of the electron (positron) and the jets do provide a good discrimination between Dirac and Majorana. The best discriminating variable from this study is the  $\theta$  angle between the reconstructed HNL and the electron (positron), where the differences between the Majorana channel (LNC + LNV) and the Dirac channel (LNC) can reach  $\mathcal{O}(35\%)$ . It also appears that the discrimination between Dirac and Majorana tends to decrease as the HNL mass increases, for a fixed coupling of  $V_{eN} = 10^{-3}$ . At this point, the reason why this behaviour is occurring is not well understood, and this is left as an open question for future studies.

One final variable worth looking at is the HNL decay length, as it is expected that a factor of two separates Dirac from Majorana HNLs due to LNV processes being allowed in the latter case. Figure [28] shows the normalized distribution of decay length of Dirac and Majorana HNLs at the generator level. A direct measurement of the decay length (or of the lifetime) of the HNL can be used together with the total cross-section to distinguish between the Dirac or Majorana nature of the HNL, provided that the HNL mass is known [24].



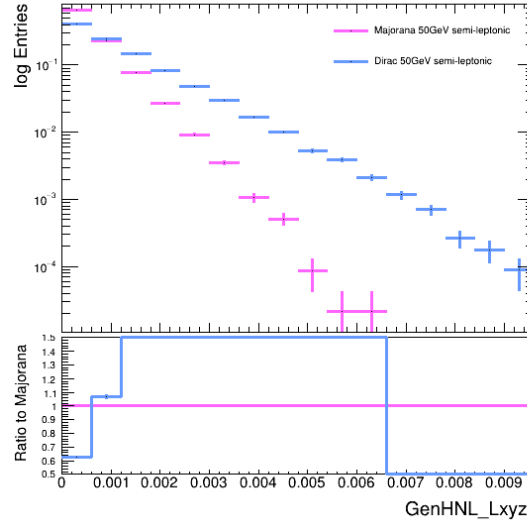


Figure 28 Decay length for Dirac (blue) and Majorana (pink) HNLs of mass  $m_N = 50$  GeV and coupling  $|V_{eN}| = 10^{-3}$  at generator level.

#### 4.2.3 Outlook

This study is one of the first to look for potential experimental differences between Dirac and Majorana HNLs in the semi-leptonic channel at the FCC-ee. Here are some suggestions in order to improve the work that was done. First, an extension of this study towards different couplings would allow a better understanding of the range of mass/coupling where the FCC-ee has the potential for distinguishing the Dirac from the Majorana nature of HNLs. Second, testing different variations for the jets algorithms, as well as assessing the smearing of the detector's response in the FCC framework would allow to carry this analysis first at generator level, and then check how the detector's response affects the discrimination power. Third, the implementation of a more sophisticated discriminant using deep neural networks

would without doubt show some interesting results. Finally and without surprise, carrying on with this analysis by including more mixing channels and more HNLs will be paramount in order to fully cover the FCC-ee's capacity on investigating the nature of HNLs.

## 5 Conclusion

The FCC-ee is expected to produce about  $10^{12}$  Z-bosons within a four year period. This very large amount of statistics allows for rare events to be probed, such as HNLs in the case of this study. The discovery potential of HNLs at the FCC-ee in the semi-leptonic channel, as well as our capacity to distinguish Dirac from Majorana HNLs experimentally using the FCC framework were explored in this thesis. Both of these studies used simulated data based on the Type I Seesaw model for one single HNL mixing with electron neutrinos only.

The sensitivity study aimed at identifying efficient event selections based on the signal significance. Event selections were optimized for masses of  $m_N = 20, 50$  and  $70$  GeV and coupling  $V_{eN} = 10^{-3}$ , with the signal and background events normalized to an integrated luminosity of  $10 \text{ fb}^{-1}$ . The main results of this analysis are two contour plots showing the signal significance for HNL masses in the range  $m_N = 10 - 80$  GeV and couplings in the range  $|V_{eN}|^2 = 10^{-4} - 10^{-10}$ , for integrated luminosities of  $10 \text{ fb}^{-1}$  and  $150 \text{ ab}^{-1}$ , the latter corresponding to the expected integrated luminosity of the FCC-ee.

The Dirac vs. Majorana analysis was performed in the semi-leptonic channel for masses of  $20, 50$  and  $70$  GeV and coupling  $V_{eN} = 10^{-3}$ . Several jet-related kinematic variables were defined at the reconstructed level, in order to look for distinctions

between Dirac and Majorana HNLs, which amounts to finding variables sensitive to LNV. As a result, the  $\theta$  angle between the HNL and the prompt lepton, as well as jet and electron energy distributions have shown strong discrimination power for masses below 80 GeV.

## Appendix A : MG5 card for HNL generation

The following code is an example for an MG5 proc. card for generating Dirac HNLs processes.

```

set default_unset_couplings 99
set group_subprocesses Auto
set ignore_six_quark_processes False
set loop_optimized_output True
set loop_color_flows False
set gauge unitary
set complex_mass_scheme False
set max_npoint_for_channel 0
import model sm
define p = g u c d s b t u~ c~ d~ s~ b~ t~
define j = g u c d s b t u~ c~ d~ s~ b~ t~
define l+ = e+ mu+
define l- = e- mu-
define vl = ve vm vt
define vl~ = ve~ vm~ vt~
import model SM_HeavyN_Dirac_CKM_Masses_LO
define e = e+ e-
define nue = ve ve~
generate e+ e- > n1~ ve , (n1~ > e+ j j)
add process e+ e- > n1 ve~ , (n1 > e- j j )
output HNL_Dirac_ejj_10GeV_1e-4Ve
launch HNL_Dirac_ejj_10GeV_1e-4Ve
done
# set to electron beams (0 for ele , 1 for proton)
set lpp1 0
set lpp2 0
set ebeam1 45.594
set ebeam2 45.594
set no_parton_cut
# Here set mass of the electron HNL
set mn1 10
# set mass of muon HNL, made heavy here
set mn2 10000
# set mass of tau HNL, made heavy here
set mn3 10000
# set electron mixing angle
set ven1 1e-4
set WN1 auto
set time_of_flight 0
set nevents 100000
done

```

## Appendix B : MG5 card for 4-body background

The following code is an example for an MG5 proc. card for generating 4-body background processes.

```
set default_unset_couplings 99
set group_subprocesses Auto
set ignore_six_quark_processes False
set loop_optimized_output True
set loop_color_flows False
set gauge unitary
set complex_mass_scheme False
set max_npoint_for_channel 0

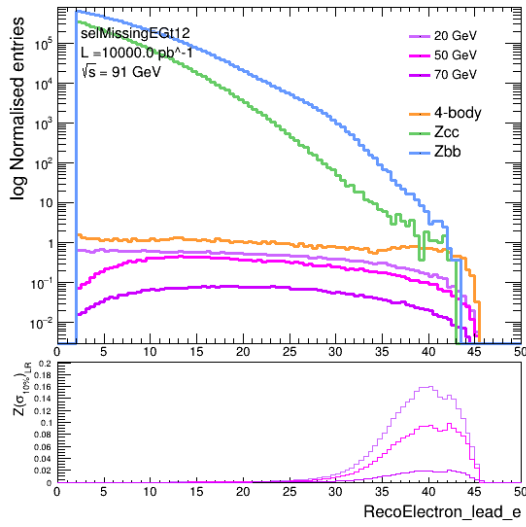
import model sm
define p = g u c d s u~ c~ d~ s~ b b~
define j = g u c d s u~ c~ d~ s~ b b~
define l+ = e+ mu+
define l- = e- mu-
define vl = ve vm vt
define vl~ = ve~ vm~ vt~
define vlp = vl vl~
define e = e+ e-

generate e+ e- > e vlp j j
output enuqq
launch enuqq
done
set nevents 100000
set ptj 0
set ptl 0
set etal 5
set mmjj 5
set drjj 0
set drjl 0
set maxjetflavor 5
set lpp1 0
set lpp2 0
set ebeam1 45.8
set ebeam2 45.8
set time_of_flight 1
done
```

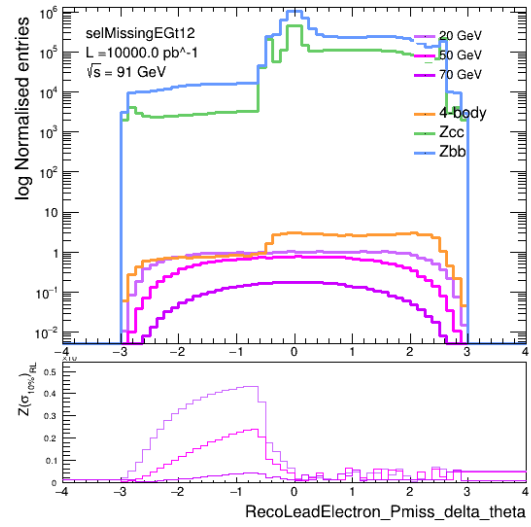
## Appendix C : Event selection distributions

The following figures show the distributions of the selected variables after each subsequent selection.

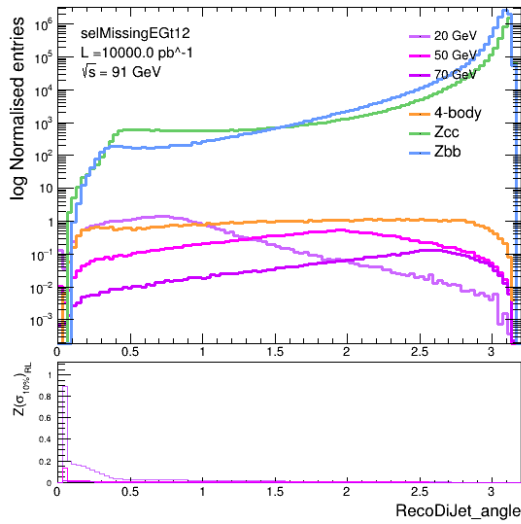
$$\cancel{E} > 12 \text{ GeV}$$



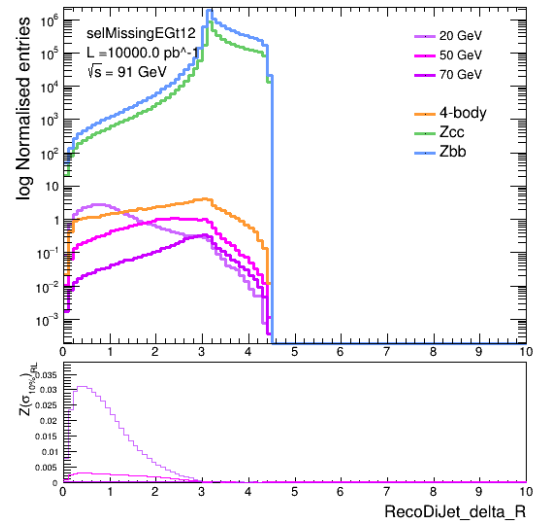
(a) Leading electron energy.



(b)  $\Theta$  between electron and  $\cancel{E}$ .

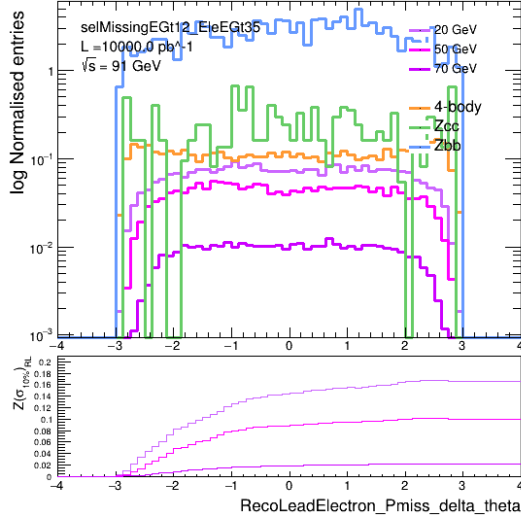
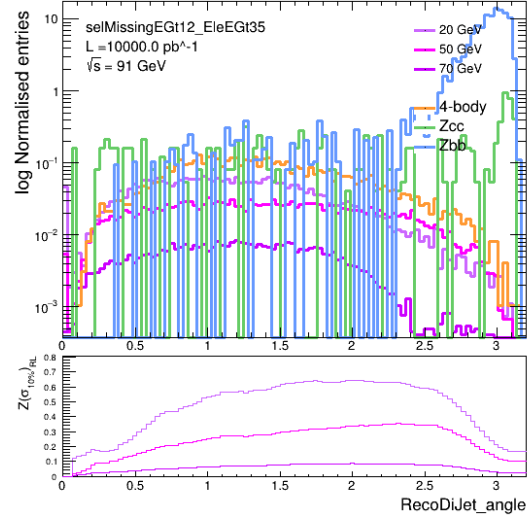


(c) 3D angle between the two jets.

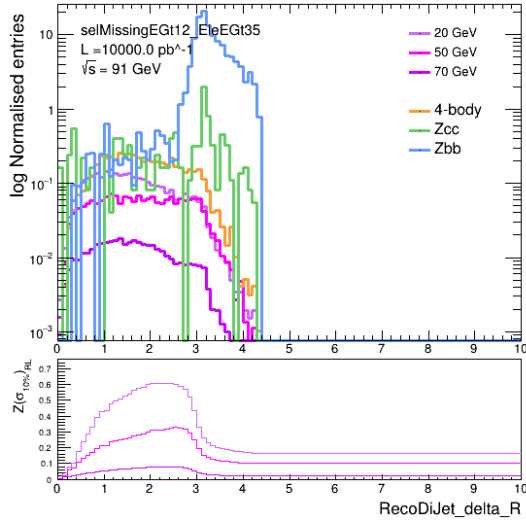
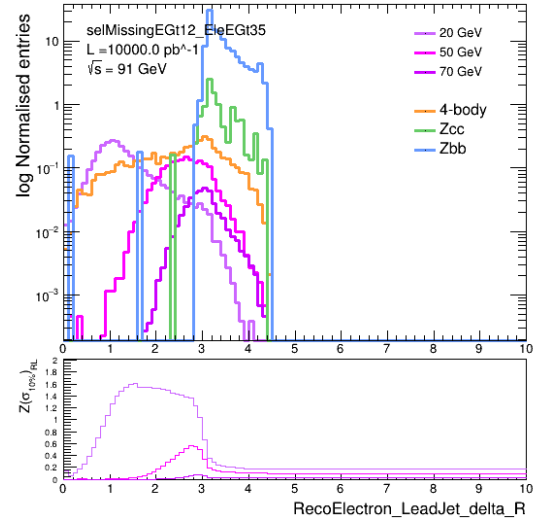


(d)  $\Delta R$  between the two jets.

$$\cancel{E} > 12 \text{ \& } E_{e^-} > 35$$

(a)  $\Theta$  between electron and  $\cancel{E}$ .

(b) 3D angle between the two jets.

(c)  $\Delta R$  between the two jets.(d)  $\Delta R$  between leading jet and electron.



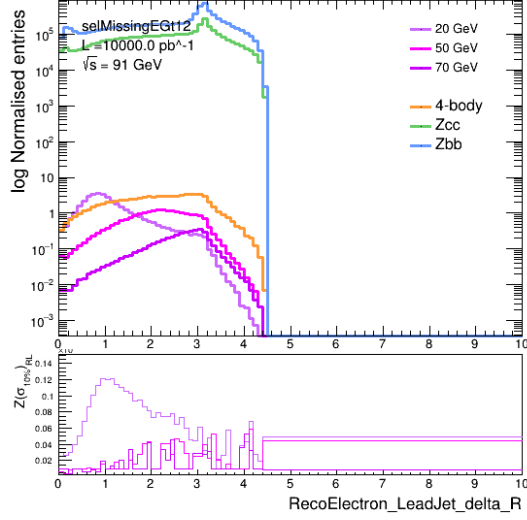
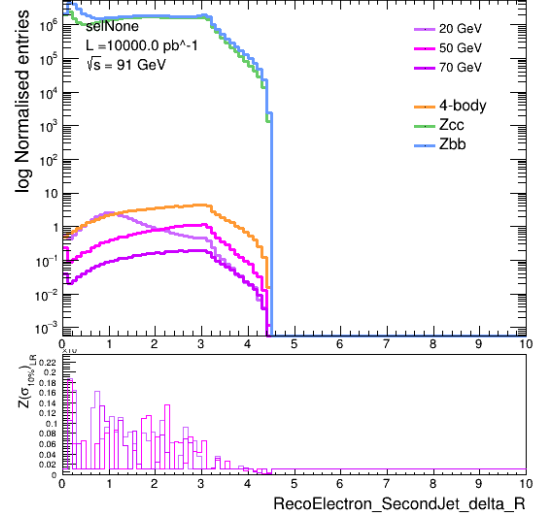
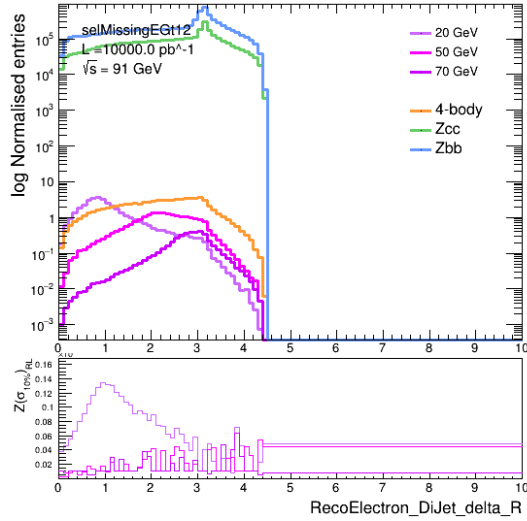
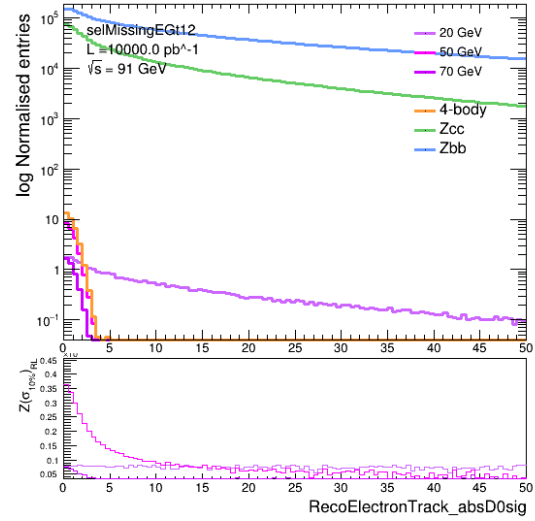
(e)  $\Delta R$  between leading jet and electron.(f)  $\Delta R$  between second jet and electron.(g)  $\Delta R$  between di-jet and electron.(h)  $\sigma_{d_0}$  for the electron tracks.

Figure 29 Distributions for the discriminating variables described in section 4.1.4, with selection  $\cancel{E} > 12$  GeV applied.

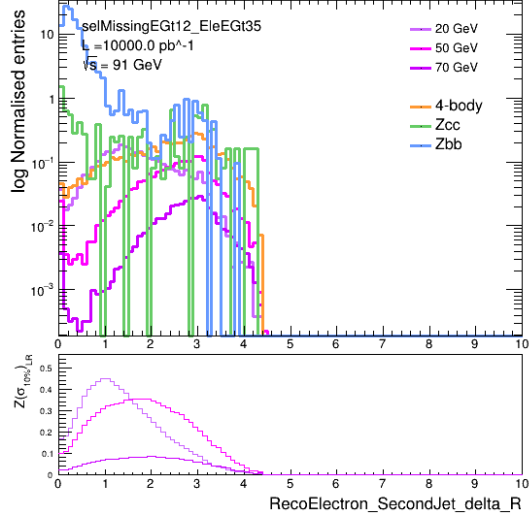
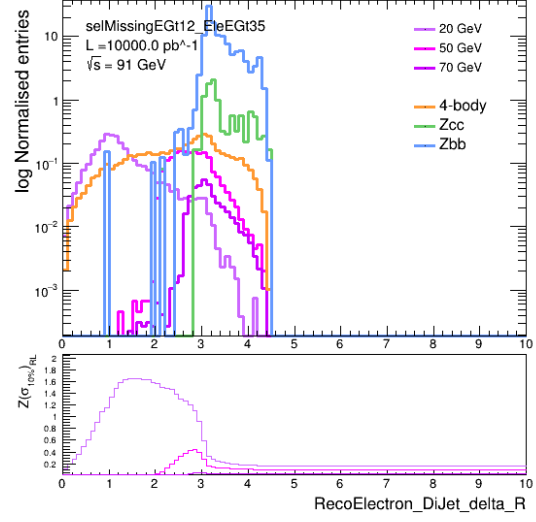
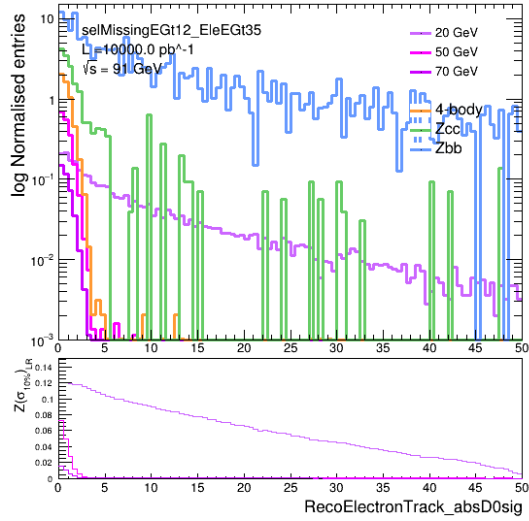
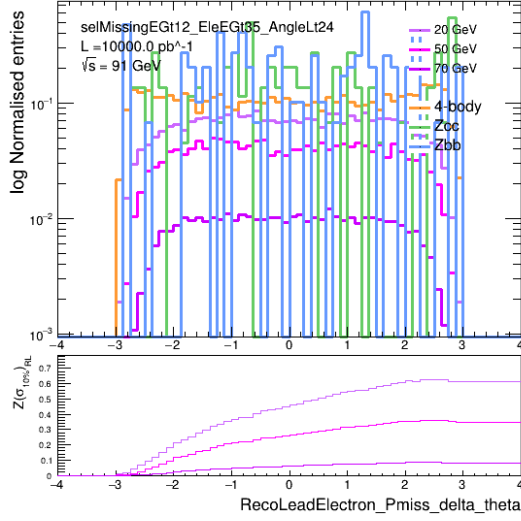
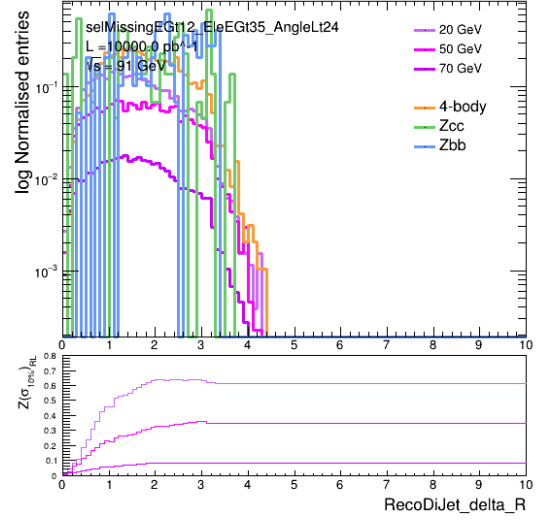
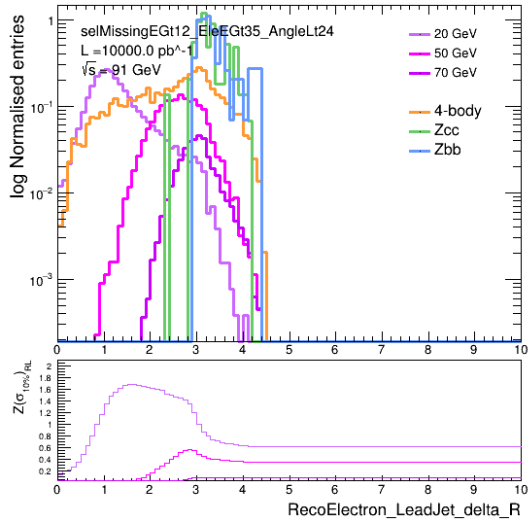
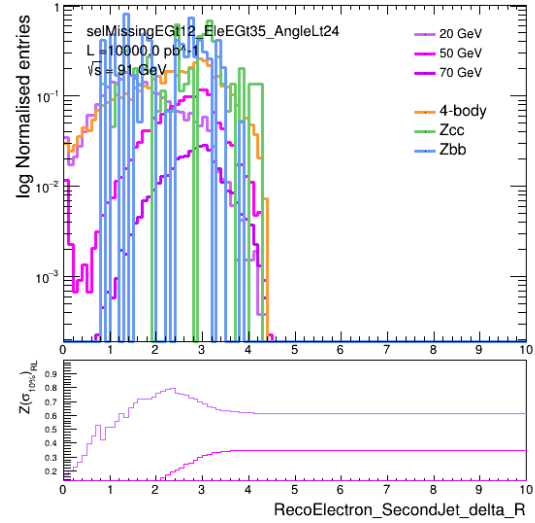
(e)  $\Delta R$  between second jet and electron.(f)  $\Delta R$  between di-jet and electron.(g)  $\sigma_{d_0}$  for the electron tracks.

Figure 30 Distributions for the discriminating variables described in section 4.1.4, with selection  $\cancel{E} > 12$  &  $E_{e^-} > 35$  applied.

$$\cancel{E} > 12 \text{ \& } E_{e^-} > 35 \text{ \& Di-jet } \Psi_{3D} < 2.4$$

(a)  $\Theta$  between electron and  $\cancel{E}$ .(b)  $\Delta R$  between the two jets.(c)  $\Delta R$  between leading jet and electron.(d)  $\Delta R$  between second jet and electron.

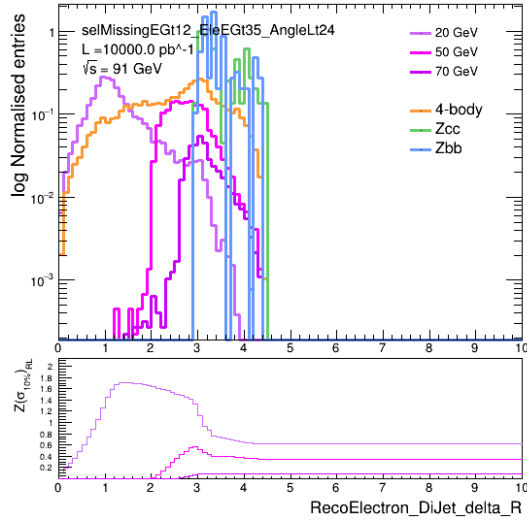
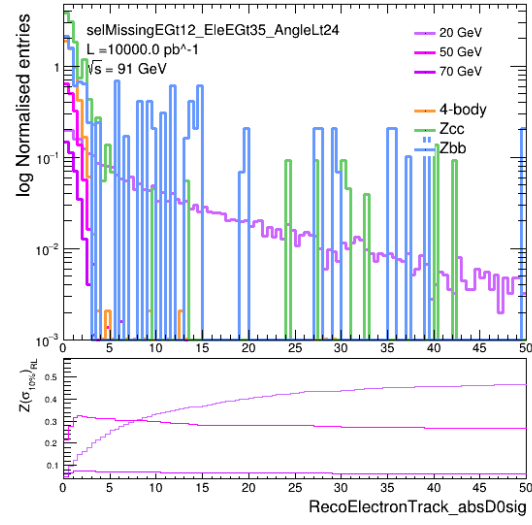
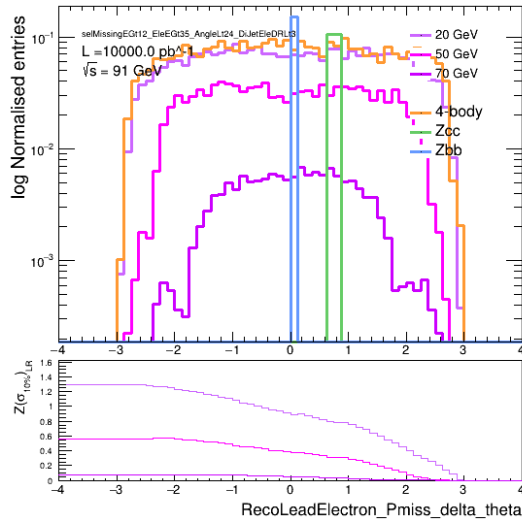
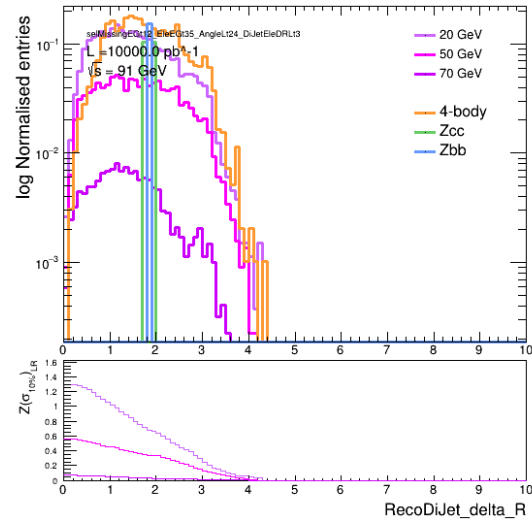
(e)  $\Delta R$  between di-jet and electron.(f)  $\sigma_{d_0}$  for the electron tracks.

Figure 31 Distributions for the discriminating variables described in section 4.1.4, with selection  $\cancel{E} > 12$  &  $E_{e^-} > 35$  &  $\Psi_{3D} < 2.4$  applied.

$$\cancel{E} > 12 \text{ \& } E_{e^-} > 35 \text{ \& Di-jet } \Psi_{3D} < 2.4 \text{ \& } \Delta R < 3$$

(a)  $\Theta$  between electron and  $\cancel{E}$ .(b)  $\Delta R$  between the two jets.

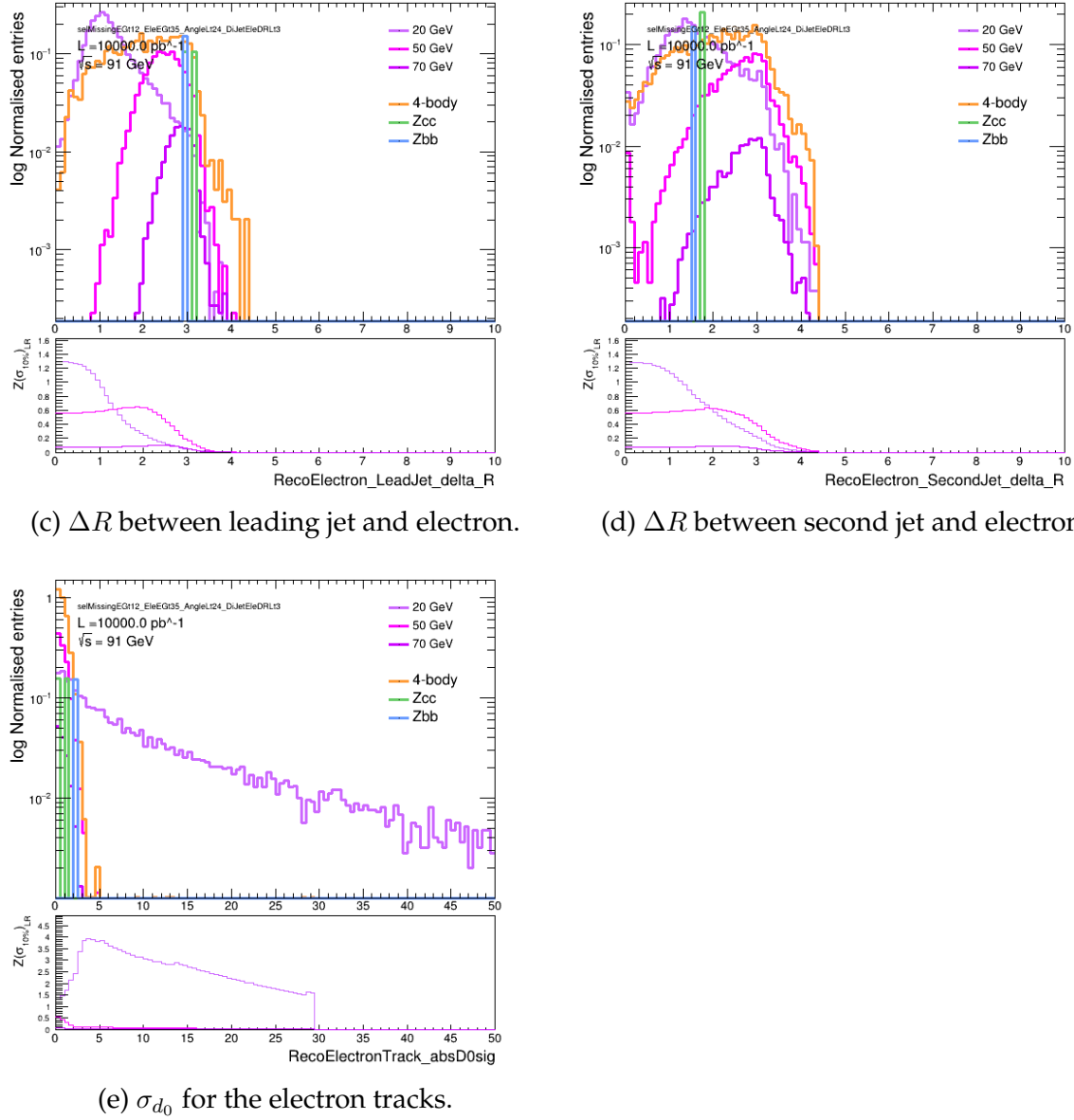


Figure 32 Distributions for the discriminating variables described in section 4.1.4, with selection  $\cancel{E} > 12$  &  $E_{e^-} > 35$  &  $\Psi_{3D} < 2.4$  &  $\Delta R < 3$  applied.

# References

- [1] Winter2023 IDEA. [http://fcc-physics-events.web.cern.ch/fcc-physics-events/FCCee/winter2023/Delphesevents\\_IDEA.php](http://fcc-physics-events.web.cern.ch/fcc-physics-events/FCCee/winter2023/Delphesevents_IDEA.php).
- [2] Formulae for Estimating Significance. <https://cds.cern.ch/record/2736148>, 2020.
- [3] ABADA, A., ET AL. FCC-ee : The Lepton Collider. *The European Physical Journal Special Topics* 228, 2 (June 2019), 261–623. <https://doi.org/10.1140/epjst/e2019-900045-4>.
- [4] ABDULLAHI, A. M., ET AL. The Present and Future Status of Heavy Neutral Leptons. *Journal of Physics G : Nuclear and Particle Physics* 50, 2 (Feb. 2023), 020501. <http://arxiv.org/abs/2203.08039>.
- [5] AGRAWAL, P., ET AL. Feebly-Interacting Particles :FIPs 2020 Workshop Report. *The European Physical Journal C* 81, 11 (Nov. 2021), 1015. <http://arxiv.org/abs/2102.12143>.
- [6] ALIMENA, J., ET AL. Searches for Long-Lived Particles at the Future FCC-ee. *Frontiers in Physics* 10 (Sept. 2022), 967881. <http://arxiv.org/abs/2203.05502>.

- [7] ALVA, D., HAN, T., AND RUIZ, R. Heavy Majorana Neutrinos from  $W\gamma$  Fusion at Hadron Colliders. *Journal of High Energy Physics* 2015, 2 (Feb. 2015), 72. <http://arxiv.org/abs/1411.7305>.
- [8] ALWALL, J., FREDERIX, R., FRIXIONE, S., HIRSCHI, V., MALTONI, F., MATTELAER, O., SHAO, H.-S., STELZER, T., TORRIELLI, P., AND ZARO, M. The automated computation of tree-level and next-to-leading order differential cross sections, and their matching to parton shower simulations. *Journal of High Energy Physics* 2014, 7 (July 2014), 79. <http://arxiv.org/abs/1405.0301>.
- [9] ANTUSCH, S., CAZZATO, E., AND FISCHER, O. Sterile neutrino searches at future  $e^+e^-$ ,  $pp$ , and  $e^-p$  colliders. *International Journal of Modern Physics A* 32, 14 (May 2017), 1750078. <http://arxiv.org/abs/1612.02728>.
- [10] ANTUSCH, S., AND FISCHER, O. Testing sterile neutrino extensions of the Standard Model at future lepton colliders. *Journal of High Energy Physics* 2015, 5 (May 2015), 53. <http://arxiv.org/abs/1502.05915>.
- [11] AOYAMA, T., KINOSHITA, T., AND NIO, M. Theory of the Anomalous Magnetic Moment of the Electron. *Atoms* 7, 1 (Mar. 2019), 28. <https://www.mdpi.com/2218-2004/7/1/28>.
- [12] ATRE, A., HAN, T., PASCOLI, S., AND ZHANG, B. The Search for Heavy Majorana Neutrinos. *Journal of High Energy Physics* 2009, 05 (May 2009), 030–030. <http://arxiv.org/abs/0901.3589>.
- [13] BENEDIKT, M., BLONDEL, A., BRUNNER, O., CAPEANS GARRIDO, M., CERUTTI, F., GUTLEBER, J., JANOT, P., JIMENEZ, J. M., MERTENS, V., MILANESE, A., OIDE, K., OSBORNE, J. A., OTTO, T., PAPAPHILIPPOU, Y., POOLE, J., TAVIAN, L. J., AND ZIMMERMANN, F. Future Circular Collider - European Strategy Update Documents. <http://cds.cern.ch/record/2653669>, 2019.

- [14] BLONDEL, A., DE GOUVÊA, A., AND KAYSER, B. Z-Boson Decays into Majorana or Dirac (Heavy) Neutrinos. *Physical Review D* 104, 5 (Sept. 2021), 055027. <http://arxiv.org/abs/2105.06576>.
- [15] BRUN, R., RADEMAKERS, F., CANAL, P., NAUMANN, A., COUET, O., MONETA, L., VASSILEV, V., LINEV, S., PIPARO, D., GANIS, G., BELLENOT, B., GUIRAUD, E., AMADIO, G., WVERKERKE, MATO, P., TIMURP, TADEL, M., WLAV, TEJEDOR, E., BLOMER, J., GHEATA, A., HAGEBOECK, S., ROISER, S., MAR-SUPIAL, WUNSCH, S., SHADURA, O., BOSE, A., CRISTINACRISTESCU, VALLS, X., AND ISEMAN, R. Root-project/root : V6.18/02. Zenodo, Aug. 2019. <https://zenodo.org/record/3895860>.
- [16] CACCIARI, M., SALAM, G. P., AND SOYEZ, G. FastJet user manual. *The European Physical Journal C* 72, 3 (Mar. 2012), 1896. <http://arxiv.org/abs/1111.6097>.
- [17] CATANI, S., DOKSHITZER, YU. L., OLSSON, M., TURNOCK, G., AND WEBBER, B. R. New clustering algorithm for multijet cross sections in e+e- annihilation. *Physics Letters B* 269, 3 (Oct. 1991), 432–438. <https://www.sciencedirect.com/science/article/pii/037026939190196W>.
- [18] CLOWE, D., BRADAC, M., GONZALEZ, A. H., MARKEVITCH, M., RANDALL, S. W., JONES, C., AND ZARITSKY, D. A direct empirical proof of the existence of dark matter. *The Astrophysical Journal* 648, 2 (Sept. 2006), L109–L113. <http://arxiv.org/abs/astro-ph/0608407>.
- [19] COLLABORATION, S. Direct Evidence for Neutrino Flavor Transformation from Neutral-Current Interactions in the Sudbury Neutrino Observatory. *Physical Review Letters* 89, 1 (June 2002), 011301. <http://arxiv.org/abs/nucl-ex/0204008>.



- [20] COLLABORATION, T. S.-K., AND ET AL, Y. F. Evidence for oscillation of atmospheric neutrinos. *Physical Review Letters* 81, 8 (Aug. 1998), 1562–1567. <http://arxiv.org/abs/hep-ex/9807003>.
- [21] DE FAVEREAU, J., DELAERE, C., DEMIN, P., GIAMMANCO, A., LEMAÎTRE, V., MERTENS, A., AND SELVAGGI, M. DELPHES 3, A modular framework for fast simulation of a generic collider experiment. *Journal of High Energy Physics* 2014, 2 (Feb. 2014), 57. <http://arxiv.org/abs/1307.6346>.
- [22] DEGRANDE, C., MATTELAER, O., RUIZ, R., AND TURNER, J. Fully-Automated Precision Predictions for Heavy Neutrino Production Mechanisms at Hadron Colliders. *Physical Review D* 94, 5 (Sept. 2016), 053002. <http://arxiv.org/abs/1602.06957>.
- [23] DODELSON, S., AND WIDROW, L. M. Sterile Neutrinos as Dark Matter. *Physical Review Letters* 72, 1 (Jan. 1994), 17–20. <http://arxiv.org/abs/hep-ph/9303287>.
- [24] DREWES, M. Distinguishing Dirac and Majorana Heavy Neutrinos at Lepton Colliders. In *Proceedings of 41st International Conference on High Energy Physics — PoS(ICHEP2022)* (Dec. 2022), p. 608. <http://arxiv.org/abs/2210.17110>.
- [25] EUROPEAN STRATEGY FOR PARTICLE PHYSICS PREPARATORY GROUP. Physics Briefing Book. <http://arxiv.org/abs/1910.11775>, Jan. 2020.
- [26] FUKUGITA, M., AND YANAGIDA, T. Baryogenesis without grand unification. *Physics Letters B* 174, 1 (June 1986), 45–47. <https://www.sciencedirect.com/science/article/pii/0370269386911263>.
- [27] GAUDIO, G. The IDEA detector concept for FCCee. In *Proceedings of 41st International Conference on High Energy Physics — PoS(ICHEP2022)* (Bologna, Italy, Nov. 2022), Sissa Medialab, p. 337. <https://pos.sissa.it/414/337>.

- [28] GIUNTI, C., AND LAVEDER, M. Neutrino Mixing. <http://arxiv.org/abs/hep-ph/0310238>, Oct. 2004.
- [29] GUIRAUD, E., NAUMANN, A., AND PIPARO, D. TDataFrame : Functional chains for ROOT data analyses. Zenodo, Jan. 2017. <https://zenodo.org/record/260230>.
- [30] HANNEKE, D., FOGWELL, S., AND GABRIELSE, G. New Measurement of the Electron Magnetic Moment and the Fine Structure Constant. *Physical Review Letters* 100, 12 (Mar. 2008), 120801. <https://link.aps.org/doi/10.1103/PhysRevLett.100.120801>.
- [31] KAYSER, B. Majorana neutrinos and their electromagnetic properties. *Physical Review D* 26, 7 (Oct. 1982), 1662–1670. <https://link.aps.org/doi/10.1103/PhysRevD.26.1662>.
- [32] MAKI, Z., NAKAGAWA, M., AND SAKATA, S. Remarks on the Unified Model of Elementary Particles. *Progress of Theoretical Physics* 28, 5 (Nov. 1962), 870–880. <https://academic.oup.com/ptp/article-lookup/doi/10.1143/PTP.28.870>.
- [33] MOHAPATRA, R. N. Seesaw Mechanism and Its Implications. In *SEESAW 25* (Apr. 2005), pp. 29–44. <http://arxiv.org/abs/hep-ph/0412379>.
- [34] NEMEVSEK, M., SENJANOVIC, G., AND ZHANG, Y. Warm Dark Matter in Low Scale Left-Right Theory. *Journal of Cosmology and Astroparticle Physics* 2012, 07 (July 2012), 006–006. <http://arxiv.org/abs/1205.0844>.
- [35] PASCOLI, S., RUIZ, R., AND WEILAND, C. Heavy Neutrinos with Dynamic Jet Vetoes : Multilepton Searches at  $\sqrt{s} = 14, \sim 27, \text{ and } 100 \text{ TeV}$ . *Journal of High Energy Physics* 2019, 6 (June 2019), 49. <http://arxiv.org/abs/1812.08750>.

- [36] SHAPOSHNIKOV, M. The nuMSM, leptonic asymmetries, and properties of singlet fermions. *Journal of High Energy Physics* 2008, 08 (Aug. 2008), 008–008. <http://arxiv.org/abs/0804.4542>.
- [37] SHARMA, T. *Phenomenology of Dirac and Majorana Type Heavy Neutral Leptons and Their Searches at the FCC-ee*. PhD thesis, Geneva U., 2022. <https://cds.cern.ch/record/2816135>.
- [38] SJÖSTRAND, T., ASK, S., CHRISTIANSEN, J. R., CORKE, R., DESAI, N., ILTEN, P., MRENNNA, S., PRESTEL, S., RASMUSSEN, C. O., AND SKANDS, P. Z. An Introduction to PYTHIA 8.2. *Computer Physics Communications* 191 (June 2015), 159–177. <http://arxiv.org/abs/1410.3012>.
- [39] STELZER, T., AND LONG, W. F. Automatic Generation of Tree Level Helicity Amplitudes. *Computer Physics Communications* 81, 3 (July 1994), 357–371. <http://arxiv.org/abs/hep-ph/9401258>.
- [40] VOLKL, V., MADLENER, T., GAEDE, F., SAILER, A., HELSENS, C., DECLARA, P. F., STEWART, G. A., DECONINCK, W., SMIESKO, J., FORTHOMME, L., AND STOIMENOVA. Key4hep/EDM4hep : V00-07-01. Zenodo, Oct. 2022. <https://zenodo.org/record/7221473>.